

NATIONAL INSTITUTE FOR FUSION SCIENCE

Effective Emission and Ionization Rate Coefficients of Atomic Carbons in Plasmas

Y. Ohkouchi, S. Sasaki, S. Takamura and T. Kato

(Received – May 17, 1993)

NIFS-228

June 1993

RESEARCH REPORT NIFS Series

This report was prepared as a preprint of work performed as a collaboration research of the National Institute for Fusion Science (NIFS) of Japan. This document is intended for information only and for future publication in a journal after some rearrangements of its contents.

Inquiries about copyright and reproduction should be addressed to the Research Information Center, National Institute for Fusion Science, Nagoya 464-01, Japan.

Effective emission and ionization rate coefficients of atomic carbons in plasmas

Y. Ohkouchi, S. Sasaki, S. Takamura

Department of Electrical Engineering and Electronics,
School of Engineering, Nagoya University, Nagoya, 464-01 Japan

T. Kato

National Institute for Fusion Science, Nagoya, 464-01 Japan

ABSTRACT

Effective emission and ionization rate coefficients of carbon atoms taking into account the density effects in plasmas are studied using a collisional radiative model including 31 sub-levels up to the principal quantum number $n = 4$. Atomic processes such as electron impact ionization, excitation, de-excitation and spontaneous emission, which are the dominant processes for carbon atoms generated from the wall material in fusion devices, are considered in our calculations. In a relatively high density plasma with electron density above 10^{13} cm^{-3} , the effective ionization rate coefficient increases about by a factor of four compared with that in a low density plasma at low temperatures of $\sim 10 \text{ eV}$ because of the increase of ionization from the excited states. Effective emission rate coefficients for several lines, which are useful for plasma diagnostics, are also presented.

Key words:

carbon atoms, ionizing plasmas, excitation, ionization, line emissions.

1. Introduction

Plasma-surface interaction is one of the crucial issues in fusion research from the viewpoints of the impurities evaporated or sputtered from the wall materials. Impurity concentration in a fusion plasma gives rise to serious problems such as the enhancement of radiation power loss and fuel dilution. On the contrary, cooling of edge plasma by radiation loss is expected from the viewpoint of reduction of heat load to the wall. Hence impurity control is indispensable for the realization of a fusion reactor. In future thermonuclear experimental reactor schemes, carbon composite materials are one of the candidates for the first wall since carbon is a low Z species. Therefore, it is desirable to investigate the transport of carbon atoms in edge plasmas. In this paper, ionization and excitation processes in plasmas are analyzed using a collisional radiative model in order to offer data on the effective line emission and ionization rate coefficients over a wide range of plasma parameters: $10^2 \leq n_e \leq 10^{18} \text{ cm}^{-3}$, $1 \leq T_e \leq 100 \text{ eV}$.

Generally, a corona model is applied to the ionization balance and the populations of the excited states in low density plasmas. In a corona model the transitions only between the ground state and the excited states concerned are considered. The population mechanism in high density as well as low density plasmas has been investigated by Fujimoto¹⁻⁶⁾ for three different types of plasmas: equilibrium, ionizing and recombining plasmas. In ionizing plasmas, the population densities are proportional to n^{-6} in the high density limit, where n is the principal quantum number⁴⁾. In ionization equilibrium plasmas, the ion abundances and the population densities in the high density limit are given by the Saha and Saha-Boltzmann equations, respectively. So far the population densities of hydrogen, helium and oxygen atoms/ions have been investigated with the collisional radiative model and applied to the measurement of plasma parameters¹⁻⁸⁾. Line profiles of multiplet lines at 156.1 and 165.7 nm of

neutral carbons emitted from the solar chromosphere with low density and temperature ($n_e \lesssim 10^{10} \text{ cm}^{-3}$, $T_e \lesssim 10 \text{ eV}$) have been investigated^{9,10}.

In this paper the ionization and line emission processes of carbon atoms under a wide range of plasma parameters are investigated under the condition of ionizing plasma by the collisional radiative model considering 31 sub-levels up to a principal quantum number $n = 4$. In high density plasmas ($n_e \geq 10^{13} \text{ cm}^{-3}$), the population densities do not depend on the electron density since they are determined only by collisional processes. Therefore the effective emission rate coefficients decrease as the electron density. The effective ionization rate coefficient increases with the electron density since the ionization rate coefficients from the excited states are much larger than that from the ground state. The spectral line of 909.5 nm ($2p3p(^3P_2) \rightarrow 2p3s(^3P_2)$) is widely used for the investigation of carbon transport and edge electron temperature measurement in JET¹¹), TEXTOR^{11,12}), DITE¹³) and PISCES¹⁴). Effective emission rate coefficients for lines with a wavelength in the ultra-violet to near-infrared region are presented.

2. Rate equations and atomic data

2.1. Rate equations

The excitation and ionization processes by electron impact are taken into account in our calculation. The collisional processes involving ions or neutral atoms are neglected since the temperature is low in edge plasmas (10~100 eV) and the kinetic energy of carbon atoms released from the first wall is relatively small ($\leq 10 \text{ eV}$). The population density of the i -th level of carbon atoms, $n(i)$, is described by the following rate equation:

$$\frac{dn(i)}{dt} = \left\{ \sum_{j \neq i} n_e C_{ji} n(j) + \sum_{j > i} A_{ji} n(j) \right\} - \left\{ \sum_{j \neq i} n_e C_{ij} n(i) + \sum_{j < i} A_{ij} n(i) \right\} - \sum_k n_e S_{ik} n(i) + \sum_k n_e \alpha_{ki} n_{+1}(k), \quad (1)$$

where n_e is the electron density and $n_{+1}(k)$ is the population density in the k -th level of a singly charged ion. C_{ji} is the electron impact excitation rate coefficient and A_{ji} is the transition probability from j to i . S_{ik} is the ionization rate coefficient for which a neutral atom in the i -th level is ionized into the k -th level of a singly charged ion. α_{ki} is the recombination rate coefficient for which a singly charged ion in the k -th level recombines into the i -th level of a neutral atom. We consider 31 levels summarized in Fig. 1 15). In the collisional radiative model, the population densities of the excited levels are generally assumed to be in a steady state, i.e. $dn(i)/dt = 0$. In our calculation, a steady state for all the excited levels is assumed.

Generally speaking, the population densities of the excited states of atoms in plasmas are described to be the sum of the contributions from the ground state $n(1)$ of the atom (purely ionizing plasma) and from the singly ionized ions (purely recombining plasma) ¹⁾. The carbon atoms in the edge plasma are considered to be in an ionizing plasma since the ionizing component is much larger than the recombining component. In our calculations the recombination process corresponding to the fourth term in eq. (1) is neglected. In an ionizing plasma, the ion abundance ratios of the ions with $z+1$ charge to the ions with z charge, n_{z+1}/n_z , is smaller than that in ionization equilibrium $[n_{z+1}/n_z]_{eq}$. The ions are ionized until n_{z+1}/n_z reaches $[n_{z+1}/n_z]_{eq}$ in an ionizing plasma. On the contrary, the ion abundance ratio n_{z+1}/n_z is larger than $[n_{z+1}/n_z]_{eq}$ in a recombining plasma.

[Figure 1]

2.2. Atomic data

(a) Electron impact excitation and de-excitation

The excitation processes to all the excited states from the ground state, $2p^2(3P)$, and metastable states, $2p^2(1D)$ and $2p^2(1S)$, are taken into account in our calculations. All the allowed transitions between the excited states are

considered, e.g., $2p3p(^1P) \rightarrow 2p3d(^1D)$. We also included the forbidden transitions whose initial and final states have the same configuration but different terms, e.g. $2p3p(^1P) \rightarrow 2p3p(^1S)$. There is scarce experimental data for carbon atoms. Therefore, we used two sorts of theoretical data and two types of semi-empirical formulae based on the Bethe approximation as follows. They are summarized in Table 1 according to the transitions.

[1] The theoretical cross sections calculated by Henry ¹⁶⁾ by the Close Coupling Method for the transitions between the ground state $2s^22p^2(^3P)$ and the two metastable states (1D), (1S).

[2] The theoretical calculation by L. A. Vainshtein ¹⁷⁾ by the Coulomb-Born approximation for the transition $2p^2(^3P) \rightarrow 2p3p(^3P)$.

[3] Rate coefficients calculated from Mewe's semi-empirical formula ¹⁸⁾ using the oscillator strength f_{ij} ¹⁹⁻²¹⁾ and the excitation energy E_{ij} . The formula is given by eq. (B1) in Appendix B.

[4] Rate coefficients for hydrogen-like ions derived from the Bethe approximation given by Jacobs ²²⁾. This formula was originally applied to the transitions, $\Delta n = 0$ and $\Delta l = \pm 1$, where l is the azimuthal quantum number. We adopted this formula to the transitions of $\Delta n = 0$, $\Delta l = 0$ and $\Delta L = \pm 1$, where L is the term value; e.g. $2p3p(^1S) \rightarrow 2p3p(^1P)$. This formula is given by eq. (B3) in Appendix B.

[Table 1]

The de-excitation rate coefficient by electron impact, C_{ji} , is calculated from the excitation rate coefficient C_{ij} :

$$C_{ji} = C_{ij} \frac{g_i}{g_j} \exp\left(\frac{E_{ij}}{T_e}\right), \quad (2)$$

where g_i and g_j are the statistical weights of the lower and upper levels, respectively.

(b) Electron impact ionization

The ionization processes by electron impact from all the excited states shown in Fig. 1 are taken into account in our calculations. The ionization process from the inner sub-shell is also considered, especially from the ground and the metastable states, e.g. $2s^22p^2(^3P) + e \rightarrow 2s2p^2(^2P) + 2e$. The ionization rate coefficient is estimated by Lotz's empirical formula as given by eq. (B5) in Appendix B.

(c) Spontaneous transition

Spontaneous transitions for all the allowed transitions and three forbidden transitions, $2p^2(^1D) \rightarrow 2p^2(^3P)$, $2p^2(^1S) \rightarrow 2p^2(^3P)$ and $2p^2(^1S) \rightarrow 2p^2(^1D)$, are considered. The spontaneous transition probability A_{ji} is expressed as,

$$A_{ji} = \frac{6.670 \times 10^{13}}{\lambda^2} \frac{g_i f_{ij}}{g_j}, \quad (3)$$

where λ is the wavelength of the emission line [nm]. The energy for the i -th level from the ground state E_i , the oscillator strengths f_{ij} , and the transition probabilities A_{ij} ²³⁾ are given in Tables A1-A5 in Appendix A.

3. Results

3.1. Population densities

(a) n_e -dependence

Two metastable states, $2p^2(^1D)$ and $2p^2(^1S)$, make the population density sensitive to n_e and T_e , especially for the singlet terms. In high density plasmas where $n_e > A_{i1}/C_{1i}$, the population densities of the metastable states are not

negligible compared to that of the ground state. Therefore the excitation from the metastable states are not negligible when determining the population densities of the excited states and the line intensities. In this section, we consider three simplified levels, i.e. the ground state, the metastable state and the excited (resonance) state, for modeling of the electron flows. The n_e -dependence of the population densities of carbon atoms are characterized in the following three density regimes:

[1] Low density regime (Corona regime):

The population densities of the excited states are determined by the balance between the collisional excitation rate $n_e C_{1i}$ from the ground state and the radiative transition probability. In this regime, the population densities of excited states are proportional to n_e , i.e. $n(i) = n_e C_{1i} n(1) / A_{i1}$.

[2] Intermediate regime:

The excitation and de-excitation rates are increased as n_e increases whereas the radiative transition probabilities A_{ji} are constant. Therefore collisional processes become dominant between the levels where A_{ji} is small. The radiative transition processes, however, are still dominant for the allowed transitions. In this regime, the population densities of the metastable levels are independent of n_e , while those of the resonance levels are proportional to n_e .

[3] High density regime:

All the population densities are determined by the balance of collisional processes. In this regime, population densities of all the excited levels are independent of n_e . The population densities of metastable states are decreased from that in the region (2) due to the excitation process from the metastable states.

Fig. 2(a) shows n_e -dependence of the population densities for $T_e = 20$ eV. The population densities are expressed as population density ratios $n(i)/n(1)$. A density below 10^3 cm^{-3} corresponds to the low density regime, while the densities of $10^6 \text{ cm}^{-3} \leq n_e < 10^{13} \text{ cm}^{-3}$ and $n_e \geq 10^{13} \text{ cm}^{-3}$ correspond the intermediate and the high density regimes, respectively. In an ionizing plasma as in our case, the out-flow by the excitation to higher levels and the ionization are balanced with the in-flow by the excitation from the ground state. Then the population density ratios $n(i)/n(1)$ for the metastable states $2p^2(^1D, ^1S)$ are smaller than the ratios of the statistical weight of each level. In the high density regime, the ratios $n(i)/n(1)$ for the metastable states decrease comparing to those in the intermediate region due to the increase of the excitation and ionization from the metastable states.

(b) T_e -dependence

Fig. 2(b) shows the T_e -dependence of population density ratios $n(i)/n(1)$ for $n_e = 10^{13} \text{ cm}^{-3}$. The T_e -dependences of the levels with singlet and triplet terms have different features. The population densities of the triplet terms are mainly determined by excitations from the ground state. Therefore, the T_e -dependence of these population densities has similar features to those of the excitation rate coefficients from the ground state. On the other hand, the population densities of the singlet terms are greatly affected by the excitation from the metastable states since the excitation from the ground state to levels with singlet terms is small due to the spin exchange forbidden transition. Hence the population densities of the singlet terms have similar T_e -dependence to those of the metastable levels. Those of the metastable states decrease as T_e increases since the excitation rate coefficients from the ground state to the metastable states decreases toward higher temperatures.

[Figure 2 (a),(b)]

(c) Influence of cascade transition from excited states

In this section, the cascade transitions from upper excited states as well as the transitions from the metastable and ground states are discussed. We combine the levels into five groups: (i) ground state, (ii) two metastable states, (iii) lower excited states except for the metastable states, (iv) upper excited states, and (v) ionized state. The electron in/out-flows of the collisional type are defined by,

$$n_e \sum_j C_{ji} n(j) \text{ and } n_e \sum_j C_{ij} n(i) , \quad (4)$$

respectively, while the electron in/out-flows of the radiative type are defined by,

$$\sum_{j>i} A_{ji} n(j) \text{ and } \sum_{j<i} A_{ij} n(i) . \quad (5)$$

As examples electron flows into/from the levels $2p3p(^3P)$ and $2p3s(^1P)$ are shown as percentage contributions in Figs. 3 and 4. These levels are the upper levels for the line emissions at 909.5 nm and 247.9 nm, respectively, which are the important lines for diagnostics as will be described in Section 4. As shown in Fig. 3 (a), the electron in-flow from the ground state is the dominant process for the determination of the population density of $2p3p(^3P)$ when $n_e \leq 10^{12} \text{ cm}^{-3}$. It occupies as much as ~85 % of the percentage contribution, while the rest is due to radiative transitions from the upper excited states, i.e. cascades. The cascade contribution from the upper levels is 15 % at low densities, and decrease down to a value of 5 % when $n_e \geq 10^{12} \text{ cm}^{-3}$. In the region $n_e \leq 10^{12} \text{ cm}^{-3}$, radiative transition to the lower excited states is the dominant out-flow from this level as shown in Fig. 3 (b). There is no radiative transition to the ground state since it is forbidden. Hence the population

density of this level for this density region is determined by the excitation from the ground state, the radiative transitions from the upper excited states (cascades), and radiative transitions to the lower excited states. The collisional excitation from the lower excited levels gradually increases as n_e exceeds 10^{12} cm^{-3} because of the increase in the population densities of the excited states. It occupies as much as $\sim 90\%$ as the electron densities exceed 10^{14} cm^{-3} . In this region, the dominant electron out-flows from this level are the collisional de-excitation to the lower excited states ($\sim 90\%$), and the collisional excitation to the upper excited states ($\sim 10\%$). The population density of this level is determined by the balance of collisional processes only, which results in a population density independent of electron density as shown in Fig. 2 (a). The contribution of the metastable states is negligibly small since $2p3p(^3P)$ is a triplet term. Consequently cascades from the upper states at low density region and the excitations from lower excited states at high density region are important for the determination of population densities of triplet terms.

The population density of $2p3s(^1P)$ is strongly influenced by the metastable states as shown in Fig. 4(a). In the low density region, $n_e \leq 10^3$ cm^{-3} , the excitation from the ground state and cascades are the dominant in-flows into this level. They each occupy $\sim 50\%$ of the percentage contributions. The excitations from the metastable states become greater than that from the ground states when $n_e \geq 10^3$ cm^{-3} because of the increase of population densities of the metastable state as shown in Fig. 2(a). They reach up to 60% of the percentage contributions for $10^3 \leq n_e \leq 10^{14}$ cm^{-3} . The contribution from the ground state increase for $n_e > 10^{14}$ following the decrease of the population densities of the metastable states. In the density region $n_e \leq 10^{14}$ cm^{-3} , the dominant electron out-flows from this level are radiative transitions to the metastable states as shown in Fig. 4(b). As n_e exceed 10^{14} cm^{-3} , the contributions of collisional de-excitations from upper excited states become large and reach up to $\sim 45\%$. In this region, the dominant electron out-flow is

excitation to the upper state, which occupies as much as ~90 % of the contributions as shown in Fig. 4(b). As a result, the effects of the metastable states as well as the cascade contributions from the upper states are important for the determination of population densities of the singlet terms.

[Figure 3 (a), (b)]

[Figure 4 (a), (b)]

3.2. Effective emission rate coefficients

The effective emission rate coefficient C_{em}^{eff} [cm^3/s] for line emissions from the i -th to the j -th level is defined as follows using the population densities of the upper level of the emission line, $n(i)$, and the transition probability A_{ij} :

$$C_{em}^{eff} = \frac{n(i)A_{ij}}{n_e \sum_m n(m)} . \quad (6)$$

The line intensity I_{em} is calculated with the use of C_{em}^{eff} as $I_{em} = n_e C_{em}^{eff} n_C$ [photons $cm^{-3} s^{-1}$], where $n_C = \sum n(m)$ is the density of carbon atoms. The effective emission rate coefficients C_{em}^{eff} for typical lines are shown in Fig. 5. The transitions for these lines are summarized in Table 2. Population densities of $n = 3$ and $n = 4$ levels are nearly constant for $n_e > 10^{13} cm^{-3}$ and $n_e > 10^{14} cm^{-3}$, respectively as shown in Fig. 2(a). In this density region the population densities are constant as n_e increases (high density region as discussed in Sec. 3.1). The effective emission rate coefficients C_{em}^{eff} defined by eq. (6) decrease as n_e increases. Generally, the upper levels emitting visible lines have a principal quantum number $n = 4$, while those emitting ultra-violet and near-infrared lines have $n = 3$. Therefore C_{em}^{eff} for visible lines are smaller than those for ultra-violet and near-infrared lines by two orders of magnitude. This is because in ionizing plasmas the population densities of the lower states are larger than those of the higher ones. Hence it is experimentally practical to

observe ultra-violet or near-infrared lines from $n = 3$ from the viewpoint of signal intensity.

[Figure 5, Table 2]

3.3. Line radiation power rate coefficient

In this section, the line radiation power rate coefficient P_{rad} [eV cm³/s] is calculated considering 91 line emissions. This quantity is defined as,

$$P_{\text{rad}} = \frac{\sum_i \left\{ n(i) \sum_{j < i} A_{ij} E_{ij} \right\}}{n_e \sum_m n(m)} \quad (7)$$

where E_{ij} is the energy of the line. Then line radiation power per volume is obtained by $n_e P_{\text{rad}} n_C$ [eV cm⁻³/s] for E_{ij} in eV. Fig. 6 shows the line radiation power rate coefficient P_{rad} as a function of the electron temperature. The electron temperature dependence is weak when $T_e \geq 10$ eV. The radiation power is strongly influenced by n_e - and T_e -dependence of the population densities of the triplet terms since almost all the population densities of the singlet terms except the metastable states are smaller than those of the triplet terms. The radiation power rate coefficient decreases as the electron density increases above 10^{13} cm⁻³ because the population densities are saturated.

[Figure 6]

3.4. Effective ionization rate coefficients

The effective ionization rate coefficient S^{eff} is defined as follows:

$$S^{\text{eff}} = \frac{\sum_i \left\{ n(i) \left(\sum_k S_{ik} \right) \right\}}{\sum_m n(m)} \quad (8)$$

The ionization process in an ionizing plasma is then expressed as $dn_C/dt = -n_e S_{\text{eff}} n_C$, where n_C is the density of carbon atoms. Although the effective emission rate coefficients $C_{\text{em}}^{\text{eff}}$ generally decrease as the electron density increases, the effective ionization rate coefficient S_{eff} increases with high densities since the ionization rate coefficients from excited states, S_{ik} , are much larger than that from the ground state, S_{1k} . The electron out-flows $n(i)S_{ik}$ are not negligible compared to $S_{1k}n(1)$, even through values of $n(i)$ are smaller than $n(1)$. As shown in Fig. 7, the n_e -dependence of the effective ionization rate coefficient S_{eff} is relatively large at low temperatures. The value of S_{eff} at $n_e = 10^{17} \text{ cm}^{-3}$ is greater by three times than that at $n_e = 10^{12} \text{ cm}^{-3}$ for $T_e = 10 \text{ eV}$. The n_e -dependence of the electron flows $n(i)S_{ik}$ which result in ionization is shown in Fig. 8. The electron flows for ionization are grouped into four types, i.e. (i) from the ground state, (ii) from the excited triplet states, (iii) from the excited singlet states and (iv) from the metastable states. The increase of S_{eff} where $n_e \geq 10^{13} \text{ cm}^{-3}$ is due to the increase of ionization from the excited levels. The ionization from the metastable states is about 20 % at low density ($10^3 \leq n_e \leq 10^{13} \text{ cm}^{-3}$) but the effect is not large. It was found that the density effects on the effective ionization rate coefficient should be considered at electron densities greater than 10^{13} cm^{-3} .

[Figure 7, 8]

4. Applications

4.1. Measurement of neutral impurity influx

The ratio of the effective ionization rate coefficient to the effective emission rate coefficient, $S_{\text{eff}}/C_{\text{em}}^{\text{eff}}$, is extensively used for the measurement of impurity influx generated from the wall and limiter through evaporation and sputtering²⁵⁾. The impurity influx is calculated from the C I emission radial profile considering both ionization and emission processes. The neutral carbon flux is attenuated through ionization. The line emission signal $I_C(z)$ observed

in the direction perpendicular to the beam, where z , the position along the beam as shown in Fig. 9, is given by,

$$I_C(z) = n_e(z) C_{em}^{eff} n_C(z) \frac{\Omega}{4\pi} V \eta . \quad (9)$$

Here Ω , V and η are the solid angle, the observation volume and the efficiency of the optical detection system, respectively. The beam attenuation is expressed in the following expression using the effective ionization rate coefficient S^{eff} :

$$\frac{1}{n_C} \frac{dn_C}{dz} = - n_e(z) \frac{S^{eff}}{v_C} , \quad (10)$$

where v_C is the velocity of carbon atoms. Eliminating $n_e(z)$ from eqs. (9) and (10), the density of carbon atoms $n_C(z)$ is obtained as,

$$n_C(z) = \frac{\int_z^{z_1} \frac{S^{eff}}{C_{em}^{eff}} I_C(\zeta) d\zeta}{v_C \frac{\Omega}{4\pi} V \eta} , \quad (11)$$

where z_1 is the position of the emission tail-off owing to complete attenuation of the carbon flux. It should be noted that S^{eff} and C_{em}^{eff} depend on n_e and T_e . The calculated results of S^{eff}/C_{em}^{eff} for the typical carbon lines, 909.5 nm and 247.9 nm, are shown in Fig. 9 (a) and (b), respectively. The ratios for both lines increase due to both an increase of S^{eff} and a decrease of C_{em}^{eff} in the high density region.

[Figure 9]

4.2. T_e -measurement using carbon activated spectroscopy.

The measurement of the electron temperature profile using the T_e -dependence of the ionization rate coefficient is one of the experimental applications of the effective ionization rate coefficient S^{eff} (12,26). An example of the experimental set-up of carbon activated spectroscopy using a laser blow-off beam is shown in Fig. 10. Neutral carbon and lithium beams are produced by laser blow-off using a thin film target. The emission profiles of Li I (670.8 nm) and C I (909.5 nm) lines along the beam path are observed by an Intensified CCD camera. The logarithmic differentiation of $n_C(z)$ obtained from eq. (10) is expressed as,

$$\frac{1}{n_C} \frac{dn_C}{dz} = \frac{1}{I_C(z)} \frac{dI_C(z)}{dz} - \frac{1}{n_e(z)} \frac{dn_e(z)}{dz} - \frac{1}{C_{em}^{eff}} \frac{dC_{em}^{eff}}{dT_e} \frac{dT_e}{dz} = -n_e \frac{S^{eff}}{v_C}. \quad (12)$$

Comparing eq. (12) with eq. (10), the radial profile of $S^{eff}(z)$ is obtained from the measured value of the emission signal $I_C(z)$ and the derived electron density profile $n_e(z)$, which is reconstructed from the Li I emission profile. Using the calculated T_e -dependences of S^{eff} and C_{em}^{eff} , the electron temperature profile is obtained from the derived value of $S^{eff}(z)$. Details of electron density reconstruction from the Li I emission profile are described elsewhere (26).

[Figure 10]

5. Discussions

5.1. Accuracy of atomic data

Because of the lack of atomic data, especially for electron impact excitations, many of the excitation rate coefficients are calculated by empirical formulae. The accuracy of these empirical formulae is considered to be within a factor of two for the allowed transitions and an order of magnitude for the forbidden transitions. We estimated the effects of the uncertainty of the atomic

data by comparing the results with different data, i.e. Mewe's semi-empirical formula and the theoretical calculation by Vainshtein. Fig. 11 (a) shows the C_{ij} for the $2p^2(^3P) \rightarrow 2p3p(^3P)$ transition obtained by three different methods (17,18,28). Fig. 11 (b) compares the electron density dependence of effective emission rate coefficient C_{em}^{eff} . The difference between the two kinds of atomic data is larger at low densities, while significant difference cannot be seen in the high density region ($\geq 10^{14} \text{ cm}^{-3}$). This phenomenon can be explained by the increase in the collisional flows between the excited levels and $2p3p(^3P)$. It should be noted that the reliability of the calculation greatly depends on the accuracy of the atomic data.

[Figure 11 (a),(b)]

5.2. Time dependence of population densities

The population densities have been calculated for the steady state by neglecting the recombination terms α_{ki} in this paper. Therefore, the applications of the ionization and the emission rate coefficients are limited to ionizing plasmas in a steady state. Under realistic conditions, carbon atoms move through a plasma where neither n_e nor T_e are uniform. Hence the plasma parameters are assumed to be constants within the relaxation time of the population densities.

For example, we consider relaxation in a plasma with $n_e = 10^{13} \text{ cm}^{-3}$ and $T_e = 20 \text{ eV}$. The triplet states in such plasmas have a relaxation time in the order of 10^{-8} s ($\sim 1/A_{j1}$) at $n_e < 10^{13} \text{ cm}^{-3}$. Hence the carbon in-flux measurement and T_e measurement using laser blow-off beam, described in Sec. 4, can have a good spatial resolution ($\sim 1 \text{ mm}$) since the carbon atoms with a kinetic energy of several electron volts move one millimeter within this relaxation time. On the contrary, the relaxation times for the singlet states are the order of 10^{-5} s ($\sim 1/n_e C_{j1}$) due to the small values of the transition probabilities. It should be noted that carbon atoms with several electron volt

can move about 1 cm within this time. The temporal variation of the plasma parameters during this relaxation time must be considered.

Acknowledgment

We would like to thank Drs. T. Fujimoto (Kyoto University) and K. Kadota (Plasma Science Center, Nagoya University) for valuable discussions and G. Csanak, R. E. H. Clark (Los Alamos National Laboratory) and L. A. Vainshtein (Lebedev Physical Institute) for contributing atomic data. This work was partly supported by the Grant-in-Aid of Scientific Research from Japan Ministry of Education, Science and Culture (JSPS Fellowship No. 3293).

References

- 1) T. Fujimoto: J. Phys. Soc. Jpn. **47**(1979)265.
- 2) T. Fujimoto: J. Phys. Soc. Jpn. **47**(1979)273.
- 3) T. Fujimoto: J. Phys. Soc. Jpn. **49**(1980)1561.
- 4) T. Fujimoto: J. Phys. Soc. Jpn. **49**(1980)1569.
- 5) T. Fujimoto: J. Phys. Soc. Jpn. **54**(1985)2905.
- 6) T. Fujimoto: J. Quant. Spectrosc. Radiat. Transfer **21**(1979)439.
- 7) T. Kato, K. Masai and J. Mizuno: J. Phys. Soc. Japan **52**(1983)3019.
- 8) K. Masai: *Research Report NIFS-209*,
National Institute for Fusion Science (1993).
- 9) R. A. Shine, B. W. Lites and E. G. Chipman: *Astrophys. J.* **224**(1978)247.
- 10) P. J. Mauas, E. H. Avrett and R. Loeser: *Astrophys. J.* **345**(1989)1104.
- 11) P. C. Stangeby: *J. Nucl. Mater* **176&177**(1990)51.
- 12) A. Pospieszczyk, F. Aumayr, H. L. Bay, E. Hintz, P. Leismann, Y. T. Lie,
G. G. Ross, D. Rusbüldt, R. P. Schorn, B. Schweer and H. Winter:
J. Nucl. Mater. **162-164**(1989)574.
- 13) D. H. J. Goodall, S. J. Fielding, C. S. Pitcher, J. Allen
and G. M. McCracken: *J. Nucl. Mater* **145-147**(1987)596.
- 14) Y. Ra, A. Pospieszczyk, Y. Hirooka, W. K. Leung and R. W. Conn:
J. Vac. Sci. Technol. **A8**(1990)1783.
- 15) *National Standard Reference Data Series 3*, National Bureau of Standard,
(1970) Section 3, A6I-1.
- 16) R. J. W. Henry, P. G. Burke and A.-L. Sinfailam:
Phys. Rev. **178**(1969)218.
- 17) L. A. Vainshtein: Private communication.
- 18) R. Mewe: *Astron. Astrophys.* **20**(1972)215.
- 19) G. A. Victor and V. Escalante:
Atomic Data and Nuclear Data Tables **40**(1988)203.
- 20) B. C. Fawcett: *Atomic Data and Nuclear Data Tables* **37**(1987)411.

- 21) D. Luo and A. K. Pradhan: J. Phys. B. **22**(1989)3377.
- 22) V. L. Jacobs and J. Davis: Phys. Rev. **A18**(1978)697.
- 23) *National Standard Reference Data Series 4 Volume 1*,
National Bureau of Standard (1966)30.
- 24) W. Lotz: Z. Physik **216**(1968)241.
- 25) E. Hintz and P. Bogen: J. Nucl. Mater. **128&129**(1984)229.
- 26) K. Kadota, A. Pospieszczyk, P. Bogen and E. Hintz:
IEEE Trans. Plasma Sci. **PS-12**(1984)264.
- 27) S. Sasaki, S. Takamura, Y. Uesugi, Y. Ohkouchi and K. Kadota:
Rev. Sci. Instrum., to be published.
- 28) G. Csanak, R. E. H. Clark: Private communication.

Tables and Captions

Table 1 Classification of the transitions for the excitation cross sections.

	Transitions	Reference
[1]	• $2p^2(^3P) \rightarrow 2p^2(^1D)$, • $2p^2(^3P) \rightarrow 2p^2(^1S)$, • $2p^2(^1D) \rightarrow 2p^2(^1S)$	Henry 16)
[2]	• $2p^2(^3P) \rightarrow 2p3p(^3P)$	Vainshtein ¹⁷⁾
[3]	•Allowed transitions other than [2] •Forbidden transitions from the ground and metastable states with $\Delta n \neq 0$.	Mewe 18)
[4]	• $2pnl(^{2s+1}L) \rightarrow 2pnl(^{2s+1}L')$ for $\Delta n = 0$ and $\Delta l = 0, \Delta L = \pm 1$	Jacobs 19)

Table 2 Transition and wavelength for the line emissions shown in Fig. 5.

Wavelength [nm]	Transition
165.7	$2p3s(^3P_2) \rightarrow 2p^2(^3P_2)$
247.9	$2p3s(^1P_1) \rightarrow 2p^2(^1S_0)$
477.2	$2p4p(^3P_2) \rightarrow 2p3s(^3P_2)$
538.0	$2p4p(^1P_2) \rightarrow 2p3s(^1P_2)$
909.5	$2p3p(^3P_2) \rightarrow 2p3s(^3P_2)$

Figure Captions

Fig. 1 Energy levels of carbon atoms.

Fig. 2 Electron density and temperature dependence of population densities.

(a) $T_e = 20$ eV. (b) $n_e = 10^{13}$ cm⁻³.

Fig. 3 Percentage contributions of electron in-flows and out-flows into/from $2p3p(^3P)$ at $T_e = 20$ eV. (a) in-flows into $2p3p(^3P)$. (b) out-flows from $2p3p(^3P)$. Sub-levels are grouped into five states: (i) the ground states, (ii) the two excited states, (iii) the lower excited states except the metastable states, (iv) the upper excited states and (v) the ionized states. Transition processes are shown in parenthesis, e.g. (rad.), (ex.) or (de-ex.).

Fig. 4 Percentage contributions of electron in-flows and out-flows to/from $2p3s(^1P)$. at $T_e = 20$ eV. (a) flows into $2p3s(^1P)$. (b) flows out from $2p3s(^1P)$.

Fig. 5 Effective emission rate coefficients C_{em}^{eff} for the line emissions of neutral carbon.

Fig. 6 Line radiation power rate coefficient P_{rad} . Line emissions of 91 lines are considered.

Fig. 7 Effective ionization rate coefficient S^{eff} of neutral carbon.

Fig. 8 Percentage contributions of ionizing electron flows. Transition processes are grouped into four types, i.e. (A) from the ground state, (B) from the excited triplet states, (C) from the excited singlet states and (D) from the metastable states.

Fig. 9 Ratio of the effective ionization rate coefficient S^{eff} to the effective emission rate coefficient $C_{\text{em}}^{\text{eff}}$ for line emissions of (a) 909.5 nm and (b) 247.9 nm..

Fig. 10 An example of the system for n_e and T_e measurement in the edge plasma of a tokamak.

Fig. 11 (a). Three different data for electron impact excitation rate coefficients ^{17,19,28}. (b) Effective emission rate coefficients obtained using the different excitation rate coefficients given in Fig. 11(a).

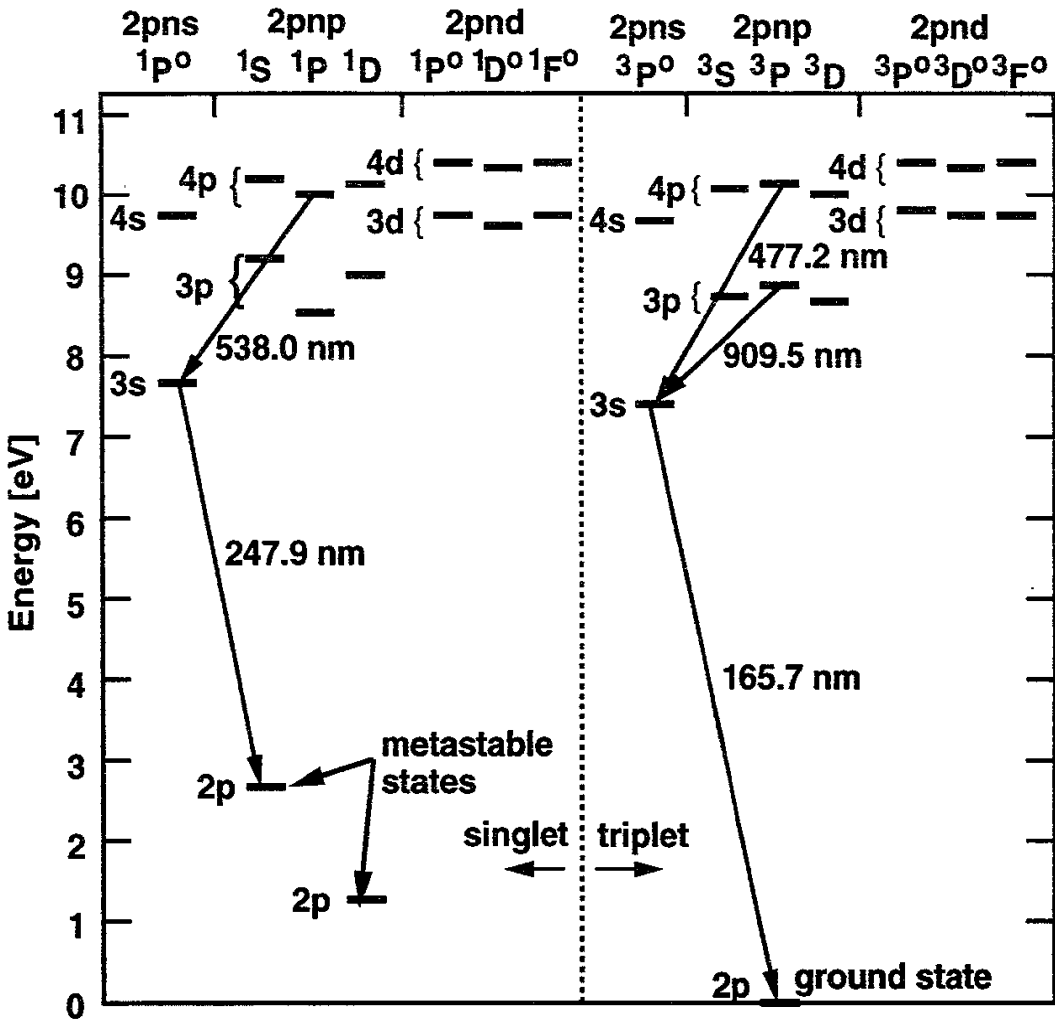


Fig. 1

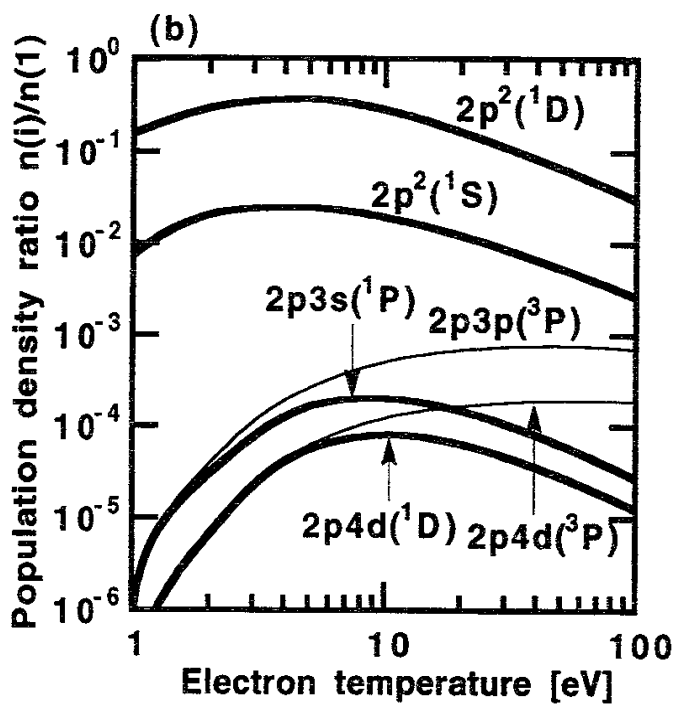
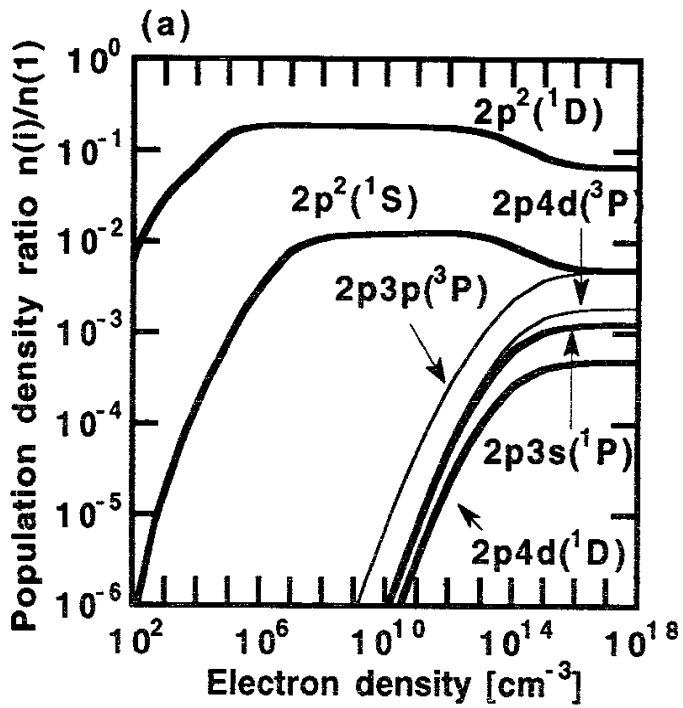


Fig. 2

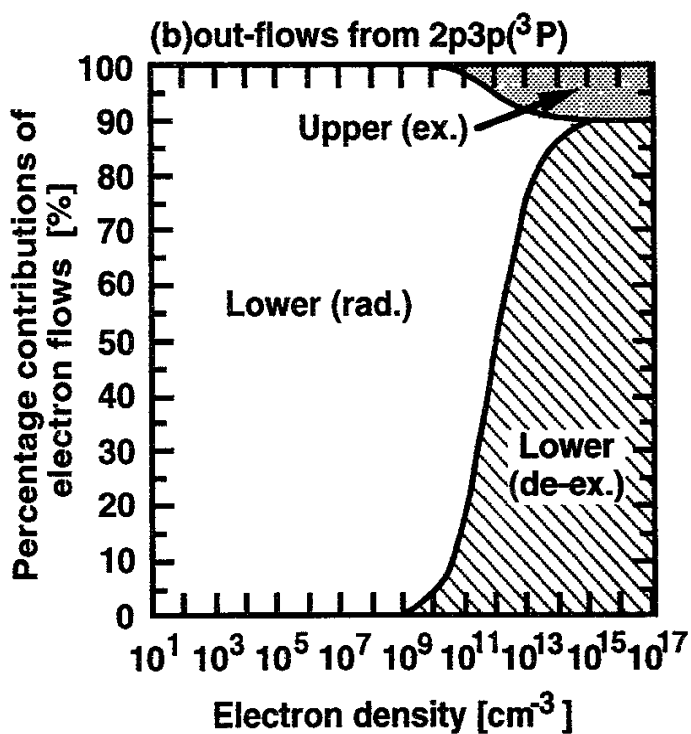
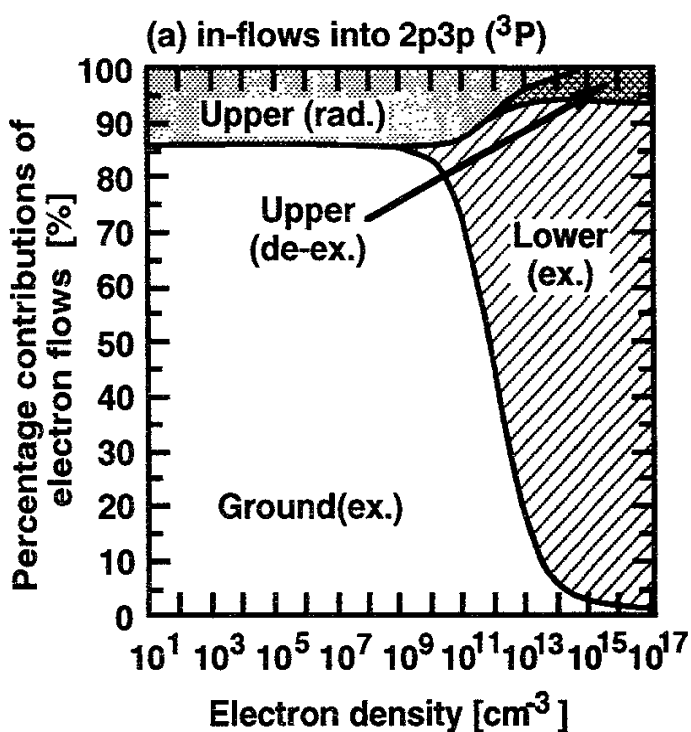


Fig. 3

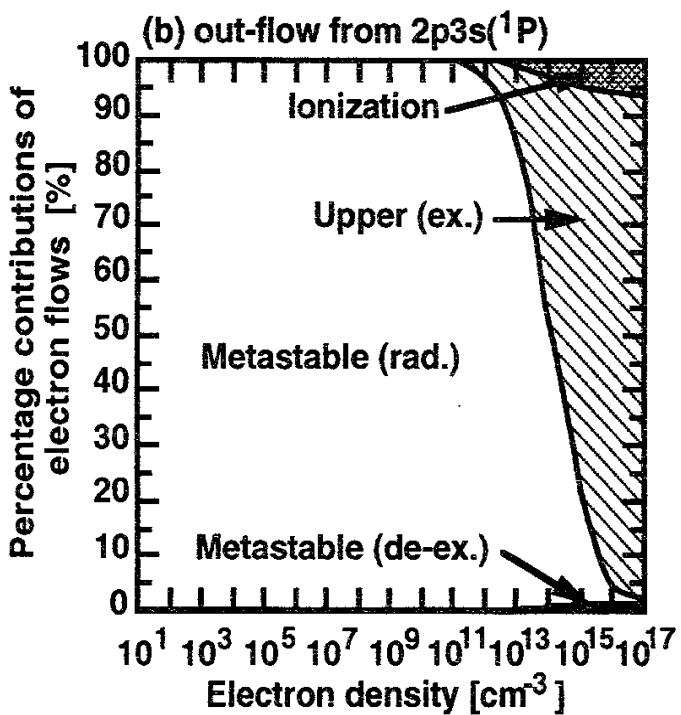
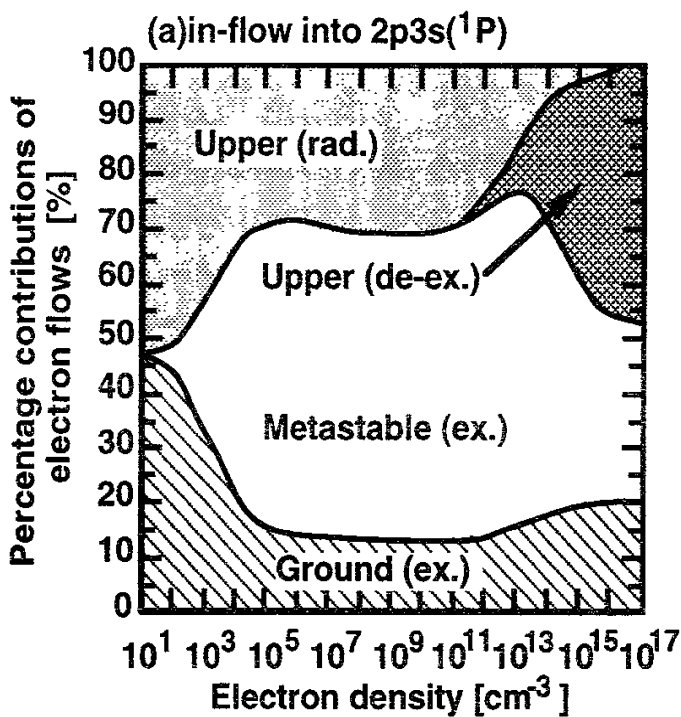


Fig. 4

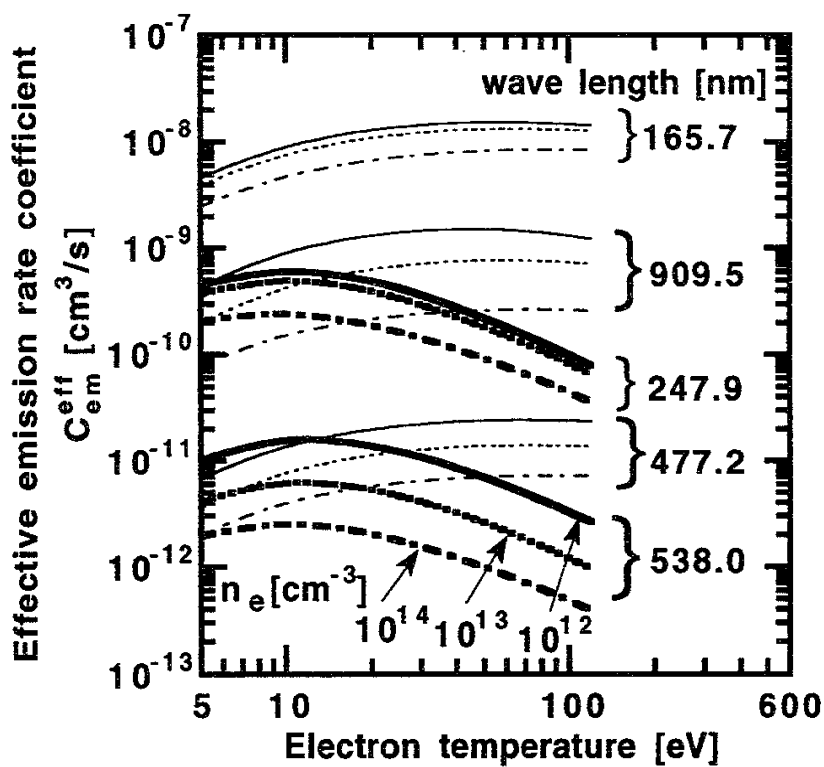


Fig. 5

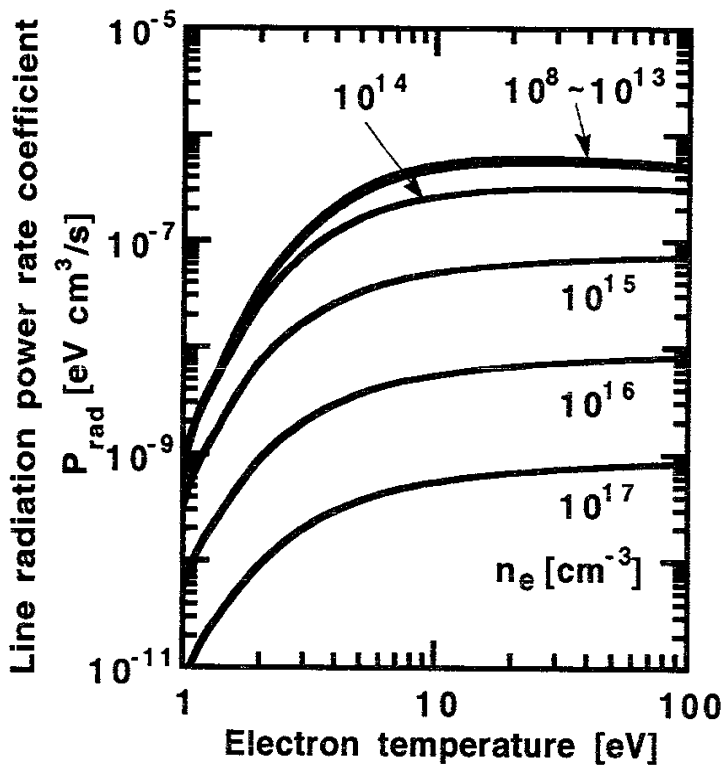


Fig. 6

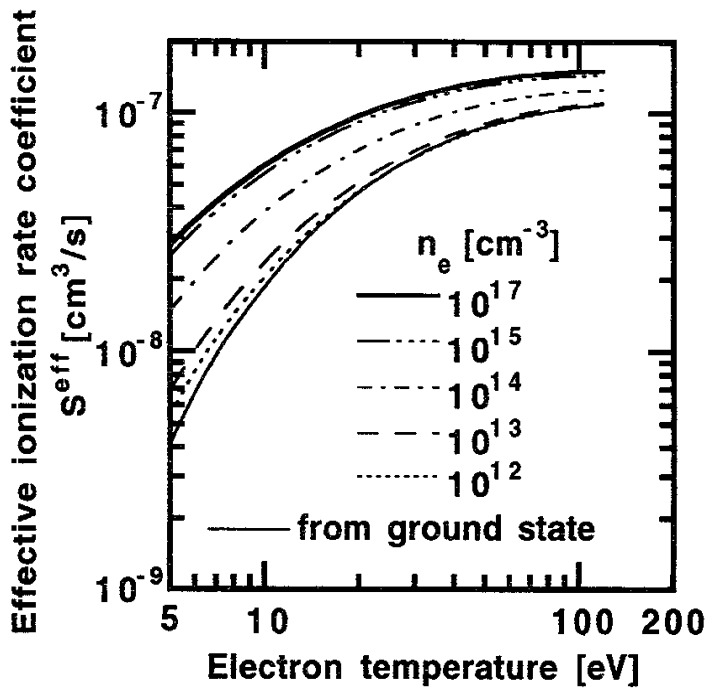


Fig. 7

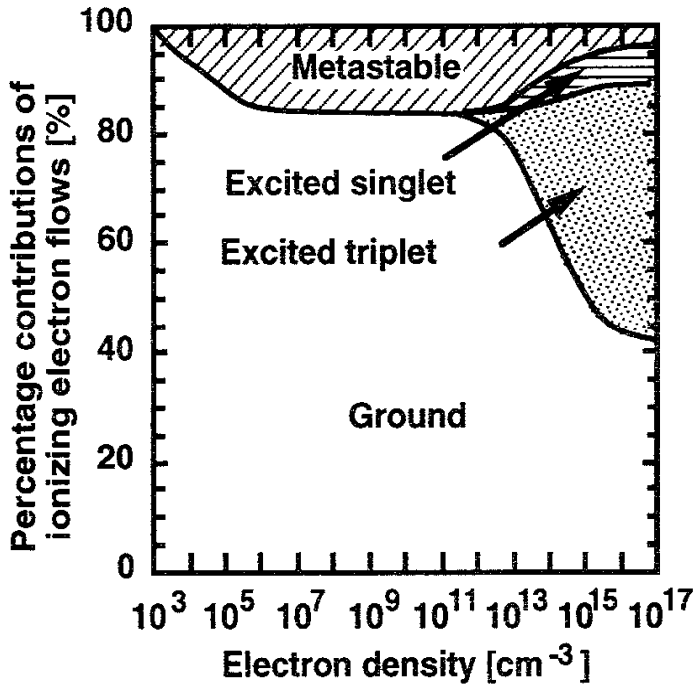


Fig. 8

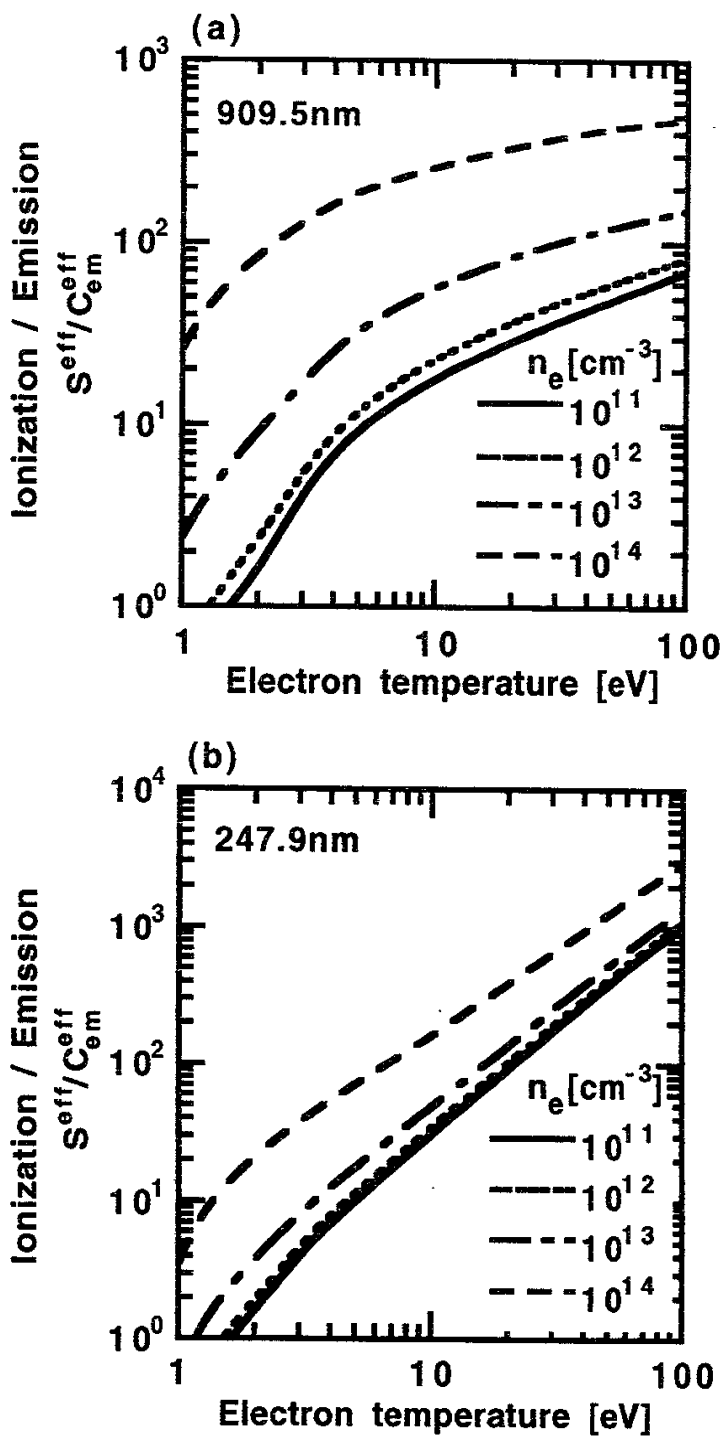


Fig. 9

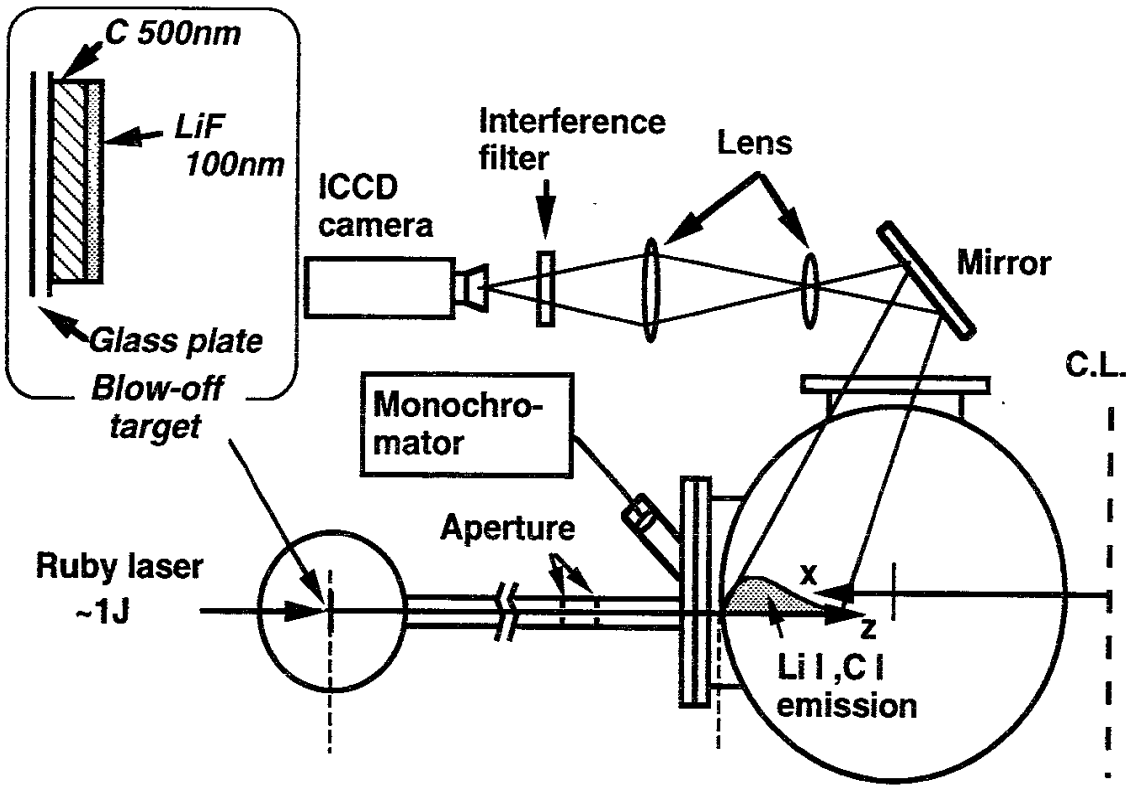


Fig. 10

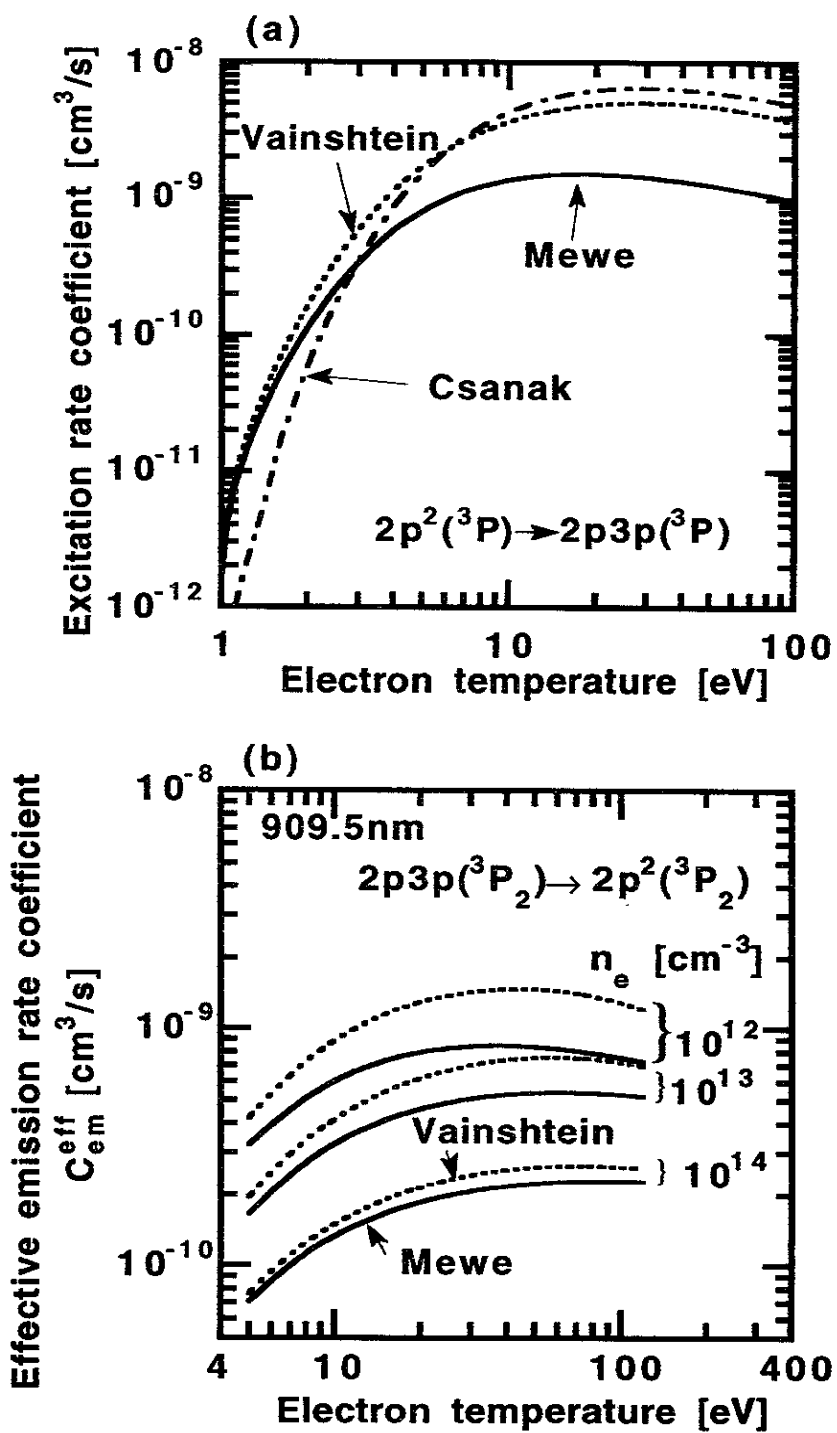


Fig. 11

Appendix A

The atomic data for the energy levels and the oscillator strengths used in this paper are summarized. Energy levels of the carbon atom and its singly charged ion are shown in Tables A1 and A2, respectively. Energy levels of the singly charged ion were taken into account for the ionization process. Transition probabilities for the forbidden and spin exchange transitions are shown in Table A3. Oscillator strengths and transition probabilities for the allowed transitions, which are required in Mewe's empirical formula eq. (B3), are shown in Table A4. In Table A5, oscillator strengths for forbidden and spin exchange transitions which are adapted in eq. (B3) are shown.

Tables

Table A1. Energy levels of a carbon atom ¹⁵).

Config.&Term	Energy[eV]	Config.&Term	Energy[eV]
2p ² (³ P)	0.00	2p3d(¹ F)	9.74
2p ² (¹ D)	1.26	2p3d(¹ P)	9.76
2p ² (¹ S)	2.68	2p3d(³ P)	9.83
2p3s(³ P)	7.49	2p4p(¹ P)	9.99
2p3s(¹ P)	7.68	2p4p(³ D)	10.00
2p3p(¹ P)	8.54	2p4p(³ S)	10.06
2p3p(³ D)	8.64	2p4p(³ P)	10.10
2p3p(³ S)	8.77	2p4p(¹ D)	10.14
2p3p(³ P)	8.85	2p4p(¹ S)	10.20
2p3p(¹ D)	9.00	2p4d(¹ D)	10.35
2p3p(¹ S)	9.17	2p4d(³ F)	10.38
2p3d(¹ D)	9.63	2p4d(³ D)	10.39
2p4s(³ P)	9.69	2p4d(¹ F)	10.41
2p3d(³ F)	9.70	2p4d(¹ P)	10.42
2p3d(³ D)	9.71	2p4d(³ P)	10.43
2p4s(¹ P)	9.71		

Table A2. Energy levels of a singly charged ion ¹⁵.

Config. & Term	Energy[eV]
2s ² 2p(2P)	0.00
2s ² 2p(4P)	5.33
2s ² 2p(2D _{3/2})	9.29
2s ² 2p(2D _{5/2})	9.29
2s ² 2p(2S)	11.96
2s ² 2p(2P)	13.71
2p ³ (4S)	17.60
2s ² 3s(2S)	14.45
2s ² 3d(2D _{3/2})	18.05
2s ² 3d(2D _{5/2})	18.05
2s ² 3p(2P)	16.33
2s ² 4f(2F)	20.95

Table A3. Transition probabilities(A) for forbidden and spin exchange transitions .

Transition	A[10 ⁸ s ⁻¹]	Ref.
2p ² (3P) - 2p ² (1D)	0.000309	23
2p ² (3P) - 2p ² (1S)	0.0026	23
2p ² (1D) - 2p ² (1S)	0.50	23

Table A4. Oscillator strengths(f) and transition probabilities(A) for allowed transitions.

Transition	f	A[10 ⁸ s ⁻¹]	Ref.
2p ² (³ P) - 2p3s(³ P)	0.1474	3.580	22
- 2p4s(³ P)	0.0217	0.883	22
- 2p3d(³ F)	0.0014	0.041	21
- 2p3d(³ D)	0.1098	2.693	22
- 2p3d(³ P)	0.0395	1.657	22
- 2p4d(³ F)	0.0008	0.0267	21
- 2p4d(³ D)	0.0591	1.661	20
- 2p4d(³ P)	0.0169	0.797	20
2p ² (¹ D) - 2p3s(¹ P)	0.1208	3.602	22
- 2p3d(¹ D)	0.01407	0.427	22
- 2p4s(¹ P)	0.01105	0.571	22
- 2p3d(¹ F)	0.09608	2.138	22
- 2p3d(¹ P)	0.00744	0.389	22
- 2p4d(¹ D)	0.0223	0.799	20
- 2p4d(¹ F)	0.1186	3.074	20
- 2p4d(¹ P)	0.0014	0.0849	20
2p ² (¹ S) - 2p3s(¹ P)	0.08545	0.309	22
- 2p4s(¹ P)	0.005149	0.0368	22
- 2p3d(¹ P)	0.1403	1.016	22
- 2p4d(¹ P)	0.1726	1.490	20
2p3s(³ P) - 2p3p(³ D)	0.4971	0.174	22
- 2p3p(³ S)	0.1071	0.231	22
- 2p3p(³ P)	0.3596	0.2903	22
- 2p4p(³ D)	0.0001	0.00017	20
- 2p4p(³ S)	0.0004	0.00344	20
- 2p4p(³ P)	0.0042	0.0123	20

Transition	f	A[10 ⁸ s ⁻¹]	Ref.
2p3s(¹ P) - 2p3p(¹ P)	0.2520	0.0794	22
- 2p3p(¹ D)	0.6367	0.288	22
- 2p3p(¹ S)	0.1213	0.349	22
- 2p4p(¹ P)	0.0120	0.012	20
- 2p4p(¹ D)	0.0132	0.0207	20
- 2p4p(¹ S)	0.0064	0.0526	20
2p3p(¹ P) - 2p3d(¹ D)	0.6960	0.217	22
- 2p4s(¹ P)	0.02234	0.0134	22
- 2p3d(¹ P)	0.2414	0.157	20
- 2p4d(¹ D)	0.0247	0.0212	20
- 2p4d(¹ P)	0.0150	0.0230	20
2p3p(³ D) - 2p4s(³ P)	0.1620	0.127	20
- 2p3d(³ F)	0.7767	0.268	20
- 2p3d(³ D)	0.1487	0.0732	22
- 2p3d(³ P)	0.0004159	0.000425	22
- 2p4d(³ F)	0.0232	0.0218	20
- 2p4d(³ D)	0.0037	0.00492	20
- 2p4d(³ P)	0.0006	0.00138	20
2p3p(³ S) - 2p4s(³ P)	0.5373	0.0652	22
- 2p3d(³ P)	0.6217	0.102	22
- 2p4d(³ P)	0.0445	0.0177	20
2p3p(³ P) - 2p4s(³ P)	0.05744	0.0175	22
- 2p3d(³ D)	0.7035	0.135	22
- 2p3d(³ P)	0.3017	0.127	22
- 2p4d(³ D)	0.0028	0.00174	20
- 2p4d(³ P)	0.0076	0.0082	20
2p3p(¹ D) - 2p3d(¹ D)	0.1159	0.0199	22

Transition	f	A[10 ⁸ s ⁻¹]	Ref.
- 2p4s(1P)	0.2274	0.0830	22
- 2p3d(1F)	0.7850	0.131	22
- 2p3d(1P)	0.00491	0.00204	22
- 2p4d(1D)	0.0005	0.00040	20
- 2p4d(1F)	0.0001	0.00006	20
2p3p(1S) - 2p4s(1P)	0.6009	0.0254	22
- 2p3d(1P)	0.5008	0.0252	22
- 2p4d(1P)	0.0061	0.00137	20
2p3d(1D) - 2p4p(1P)	0.160	0.015	20
- 2p4p(1D)	0.0438	0.00489	20
2p4s(3P) - 2p4p(3D)	0.7703	0.0221	20
- 2p4p(3S)	0.1647	0.0291	20
- 2p4p(3P)	0.5123	0.0350	20
2p3d(3F) - 2p4p(3D)	0.192	0.0120	20
2p3d(3D) - 2p4p(3D)	0.0449	0.00188	20
2p3d(3D) - 2p4p(3P)	0.131	0.0134	20
2p4s(1P) - 2p4p(1P)	0.4126	0.014	20
- 2p4p(1D)	0.8989	0.0423	20
- 2p4p(1S)	0.181	0.0554	20
2p3d(1F) - 2p4p(1D)	0.1642	0.0161	20
2p3d(1P) - 2p4p(1P)	0.0701	0.00157	20
- 2p4p(1D)	0.00483	0.00018	20
- 2p4p(1S)	0.0881	0.0218	20
2p3d(3P) - 2p4p(3D)	0.00417	0.000037	20
- 2p4p(3S)	0.0901	0.00578	20
- 2p4p(3P)	0.0708	0.00193	20
2p4p(1P) - 2p4d(1D)	0.8690	0.03	20

Transition	f	A[10 ⁸ s ⁻¹]	Ref.
- 2p4d(¹ P)	0.3055	0.0014	20
2p4p(³ D) - 2p4d(³ F)	1.035	0.0432	20
- 2p4d(³ D)	0.1907	0.0117	20
- 2p4d(³ P)	0.0118	0.0014	20
2p4p(³ S) - 2p4d(³ P)	1.2370	0.0248	20
2p4p(³ P) - 2p4d(³ D)	0.9605	0.0241	20
- 2p4d(³ P)	0.3158	0.0162	20
2p4p(¹ D) - 2p4d(¹ D)	0.1552	0.0031	20
- 2p4d(¹ F)	1.0690	0.0242	20
- 2p4d(¹ P)	0.0129	0.0007	20
2p4p(¹ S) - 2p4d(¹ P)	1.1660	0.00822	20

Table A5. Oscillator strengths for forbidden transitions used in eq. (B3).

Transition	f	Applied allowed transition
2p ² (³ P) - 2p3s(¹ P)	0.1474	2p ² (³ P) - 2p3s(³ P)
- 2p3p(¹ P)	0.0395	- 2p3d(³ P)
- 2p3p(³ D)	0.0395	- 2p3d(³ P)
- 2p3p(³ S)	0.0395	- 2p3d(³ P)
- 2p3p(³ P)	0.0395	- 2p3d(³ P)
- 2p3p(¹ D)	0.0395	- 2p3d(³ P)
- 2p3p(¹ S)	0.0395	- 2p3d(³ P)
- 2p3d(¹ D)	0.1098	- 2p3d(³ D)
- 2p4s(¹ P)	0.0217	- 2p4s(³ P)
- 2p3d(¹ F)	0.0014	- 2p3d(³ F)
- 2p3d(¹ P)	0.0395	- 2p3d(³ P)
- 2p4p(¹ P)	0.0169	- 2p4d(³ P)

Transition	f	Applied allowed transition
- 2p4p(³ D)	0.0169	- 2p4d(³ P)
- 2p4p(³ S)	0.0169	- 2p4d(³ P)
- 2p4p(³ P)	0.0169	- 2p4d(³ P)
- 2p4p(¹ D)	0.0169	- 2p4d(³ P)
- 2p4p(¹ S)	0.0169	- 2p4d(³ P)
- 2p4d(¹ D)	0.0591	- 2p4d(³ D)
- 2p4d(¹ F)	0.0008	- 2p4d(³ F)
- 2p4d(¹ P)	0.0169	- 2p4d(³ P)
2p ² (¹ D) - 2p3s(³ P)	0.1208	2p ² (¹ D) - 2p3s(¹ P)
- 2p3p(¹ P)	0.01407	- 2p3d(¹ D)
- 2p3p(³ D)	0.01407	- 2p3d(¹ D)
- 2p3p(³ S)	0.01407	- 2p3d(¹ D)
- 2p3p(³ P)	0.01407	- 2p3d(¹ D)
- 2p3p(¹ D)	0.01407	- 2p3d(¹ D)
- 2p3p(¹ S)	0.01407	- 2p3d(¹ D)
- 2p4s(³ P)	0.01105	- 2p4s(¹ P)
- 2p3d(³ F)	0.09608	- 2p3d(¹ F)
- 2p3d(³ D)	0.01407	- 2p3d(¹ D)
- 2p3d(³ P)	0.00744	- 2p3d(¹ P)
- 2p4p(¹ P)	0.0223	- 2p4d(¹ D)
- 2p4p(³ D)	0.0223	- 2p4d(¹ D)
- 2p4p(³ S)	0.0223	- 2p4d(¹ D)
- 2p4p(³ P)	0.0223	2p ² (¹ D) - 2p4d(¹ D)
- 2p4p(¹ D)	0.0223	- 2p4d(¹ D)
- 2p4p(¹ S)	0.0223	- 2p4d(¹ D)
- 2p4d(³ F)	0.1186	- 2p4d(¹ F)
- 2p4d(³ D)	0.0223	- 2p4d(¹ D)

Transition	f	Applied allowed transition
- 2p4d(³ P)	0.0014	- 2p4d(¹ P)
2p ² (¹ S) - 2p3s(³ P)	0.08545	2p ² (¹ S) - 2p3s(¹ P)
- 2p3p(¹ P)	0.1403	- 2p3d(¹ P)
- 2p3p(³ D)	0.1403	- 2p3d(¹ P)
- 2p3p(³ S)	0.1403	- 2p3d(¹ P)
- 2p3p(³ P)	0.1403	- 2p3d(¹ P)
- 2p3p(¹ D)	0.1403	- 2p3d(¹ P)
- 2p3p(¹ S)	0.1403	- 2p3d(¹ P)
- 2p3d(¹ D)	0.1403	- 2p3d(¹ P)
- 2p4s(³ P)	0.005149	- 2p4s(¹ P)
- 2p3d(³ F)	0.1403	- 2p3d(¹ P)
- 2p3d(³ D)	0.1403	- 2p3d(¹ P)
- 2p3d(¹ F)	0.1403	- 2p3d(¹ P)
- 2p3d(³ P)	0.1403	- 2p3d(¹ P)
- 2p4p(¹ P)	0.1726	- 2p4d(¹ P)
- 2p4p(³ D)	0.1726	- 2p4d(¹ P)
- 2p4p(³ S)	0.1726	- 2p4d(¹ P)
- 2p4p(³ P)	0.1726	- 2p4d(¹ P)
- 2p4p(¹ D)	0.1726	- 2p4d(¹ P)
- 2p4p(¹ S)	0.1726	- 2p4d(¹ P)
- 2p4d(¹ D)	0.1726	- 2p4d(¹ P)
- 2p4d(³ F)	0.1726	- 2p4d(¹ P)
- 2p4d(³ D)	0.1726	- 2p4d(¹ P)
- 2p4d(¹ F)	0.1726	- 2p4d(¹ P)
- 2p4d(³ P)	0.1726	- 2p4d(¹ P)

Appendix B

The approximation and semi-empirical formulae for the excitation and ionization rate coefficients by electron impact are summarized.

1) Mewe's empirical formula for excitation 18).

$$C_{ij}=1.6 \times 10^5 T_e^{-\frac{1}{2}} E_{ij}^{-1} f_{ij} P(y) \exp(-y), \quad (\text{B1})$$

$$P(y)=a+(by-cy^2+dy^3+e)\exp(y)E_1(y)+(c+d)y-dy^2, \quad (\text{B2})$$

where $y=E_{ij}/T_e$, T_e is the electron temperature and E_{ij} is the excitation energy in eV. The constant values of a, b, c, d are given as follows:

- (i) $a=0.15$, $b=c=d=0$, $e=0.276$ for allowed transition with $\Delta n=0$,
- (ii) $a=0.6$, $b=c=d=0$, $e=0.276$ for allowed transition with $\Delta n \neq 0$,
- (iii) $a=0.15$, $b=c=d=e=0$ for monopole and quadrupole transition,
- (iv) $a=b=d=e=0$, $c=0.1$ for transition with spin exchange.

The oscillator strengths f_{ij} are originally defined for allowed transitions. In the Mewe's semi-empirical formula, f_{ij} for forbidden transitions is adopted from the f_{ij} for allowed transition, which has the same initial and final states with the same principle quantum number and electron configuration. For example, the value of f_{ij} for the allowed transition, $2p^2(^3P) \rightarrow 2p3s(^3D)$, is used for the forbidden transition, $2p^2(^3P) \rightarrow 2p3s(^1P)$. The f_{ij} for the forbidden transition, $2p^2(^3P) \rightarrow 2p4p(^1P)$, however, is taken from the f_{ij} for an allowed transition, $2p^2(^3P) \rightarrow 2p4d(^3P)$. This is because the transition which has the same electron configuration, $2p^2(^3P) \rightarrow 2p4p(^3P)$, is forbidden.

2) Bethe's approximation given by Jacobs for $\Delta n = 0$ transitions of hydrogenic ions 22).

$$C_{ij} = \left(\frac{\mu}{m_e}\right)^{\frac{1}{2}} z_0^2 \frac{32\pi^2}{\sqrt{3}} \frac{a_0^3 I_H}{h/2\pi} \frac{3}{4} \frac{l_{>}}{2l+1} \left(\frac{n}{z+1}\right)^2 (n^2 - l_{>}^2) \left(\frac{I_H}{T_e}\right)^{\frac{1}{2}} \frac{\sqrt{3}}{2\pi} E_1(x)$$

$$= 6.51 \times 10^{-8} \left(\frac{\mu}{m_e}\right)^{\frac{1}{2}} \left(\frac{z_0}{z+1}\right)^2 \frac{l_{>}}{2l+1} n^2 (n^2 - l_{>}^2) \left(\frac{I_H}{T_e}\right)^{\frac{1}{2}} E_1(x), \quad (B3)$$

$$x = \left(\frac{n^2}{2(z+1)I_H}\right)^2 \frac{\mu}{m_e} \frac{I_H}{T_e} (E_{ij}^2 + \Gamma_l^2 + (h/2\pi)^2 \omega_p^2), \quad (B4)$$

where the notations are summarized as follows:

μ : reduced mass of ion,

m_e : mass of electron,

z : charge number of the target particles,

z_0 : charge number of the incident particles,

a_0 : Bohr radius,

h : Planck constant,

ω_p : plasma angular frequency,

Γ_l : energy width owing to the finite natural lifetime,

E_{ij} : excitation energy,

$E_1(y)$: exponential integral,

I_H : ionization potential of hydrogen = 13.6 eV,

$l_{>}$: larger value whether l of initial state or of final state,

T_e : electron temperature.

$z_0 = -1$ is used since we consider electron impact processes.

$z = 0$ is used for a carbon atom.

3) Lotz's formula for ionization (24).

$$S = 6.7 \times 10^7 \sum_{i=1}^N \frac{a_i \xi_i}{T_e^{3/2}} \left\{ \frac{1}{I_i/T_e} \int_{I_i/T_e}^{\infty} \frac{\exp(-x)}{x} dx - \frac{b_i \exp(c_i)}{I_i/T_e + c_i} \int_{I_i/T_e + c_i}^{\infty} \frac{\exp(-y)}{y} dy \right\}, \quad (B5)$$

where a_i , b_i , c_i are the constants given for each ions. The notations I_i and x_i are the ionization potential from the i -th sub shell and the number of equivalent electrons in i -th sub shell, respectively. It is well known that the empirical formula by Lotz is in a good agreement with experimental results especially for low Z elements like carbon. The ionization rate coefficients from excited state are calculated with I_i = ionization energy from the excited state and $a_i = 4.5 \times 10^{-14} [\text{cm}^2 \text{eV}^2]$, $b_i=c_i=0$. The values I_i are taken considering the final states of the ionized ions given in Table A2.

The excitation cross sections from different sources for the transitions listed in Table B1 are compared in Fig. B1 - B9. Cross sections given by Csanak ²⁸⁾ are theoretical calculations made by using the Distorted Wave Method.

Table B1. List of excitation cross section.

Transition	E_{ij} [eV]	Transition Type	Figure No.
$2p^2(3P) - 2p^2(1D)$	1.26	Spin Exchange	B1
$2p^2(3P) - 2p^2(1S)$	2.68	Spin Exchange	B2
$2p^2(1D) - 2p^2(1S)$	1.42	Forbidden	B3
$2p^2(3P) - 2p3p(3P)$	8.85	Forbidden	B4
$2p^2(1D) - 2p3p(3P)$	7.59	Spin Exchange	B5
$2p^2(1D) - 2p3d(1D)$	8.37	Allowed	B6
$2p^2(3P) - 2p4s(3P)$	9.69	Allowed	B7
$2p^2(1D) - 2p3p(1P)$	7.28	Forbidden	B8
$2p^2(1S) - 2p3p(3P)$	6.17	Spin Exchange	B9

Figure Captions

Fig. B1 Excitation cross section, $2p^2(3P) \rightarrow 2p^2(1D)$.

Fig. B2 Excitation cross section, $2p^2(3P) \rightarrow 2p^2(1S)$.

Fig. B3 Excitation cross section, $2p^2(1D) \rightarrow 2p^2(1S)$.

Fig. B4 Excitation cross section, $2p^2(3P) \rightarrow 2p3p(3P)$.

Fig. B5 Excitation cross section, $2p^2(1D) \rightarrow 2p3p(3P)$.

Fig. B6 Excitation cross section, $2p^2(1D) \rightarrow 2p3d(1D)$.

Fig. B7 Excitation cross section, $2p^2(3P) \rightarrow 2p4s(3P)$.

Fig. B8 Excitation cross section, $2p^2(1D) \rightarrow 2p3p(1P)$.

Fig. B9 Excitation cross section, $2p^2(1S) \rightarrow 2p3p(3P)$.

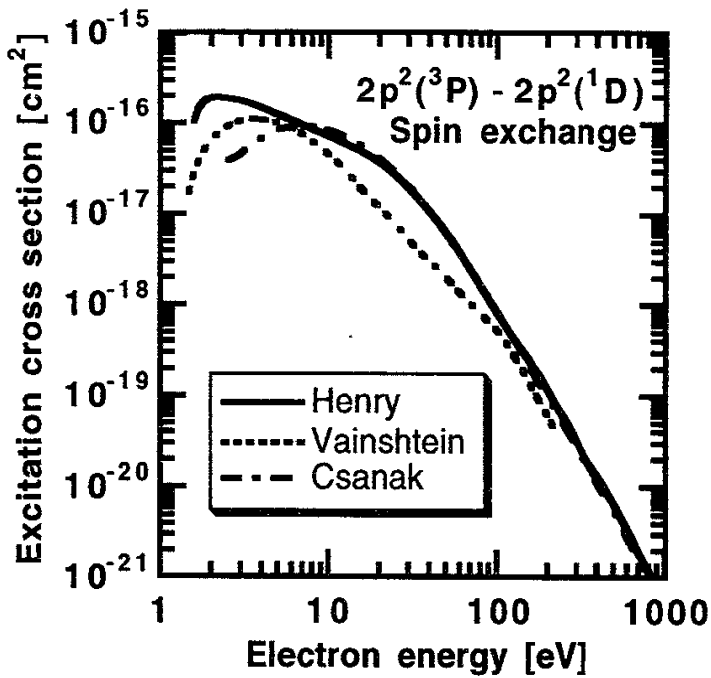


Fig. B1

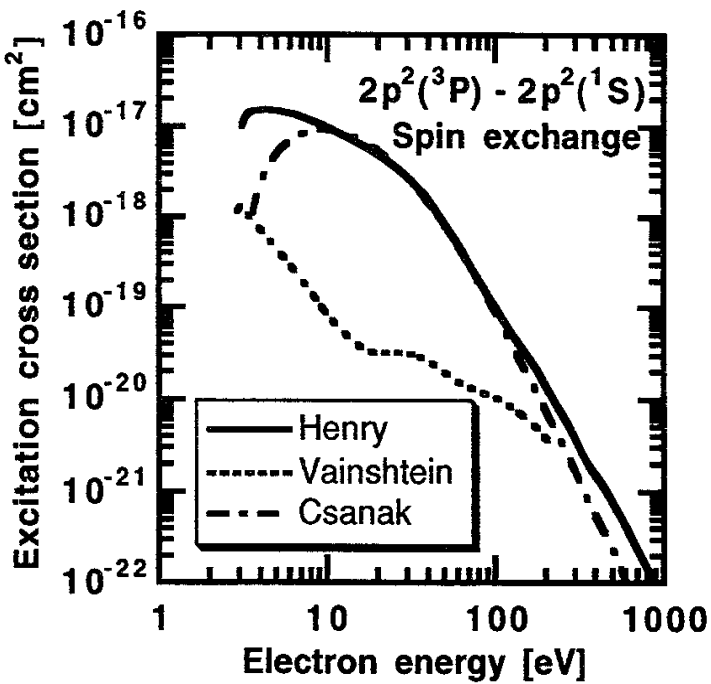


Fig. B2

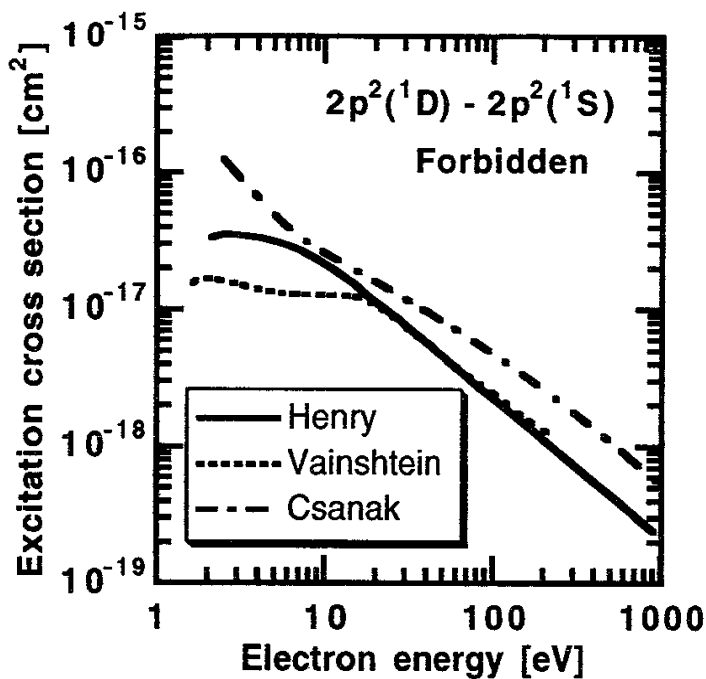


Fig. B3

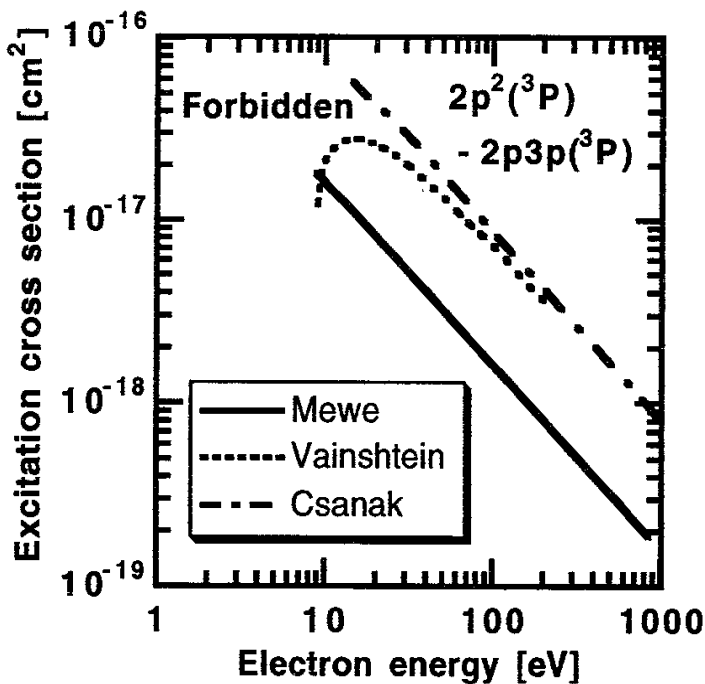


Fig. B4

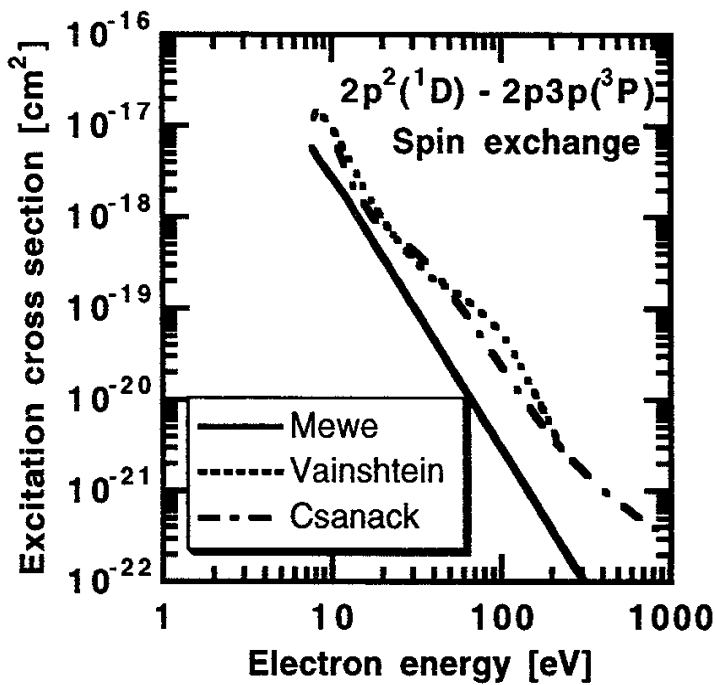


Fig. B5

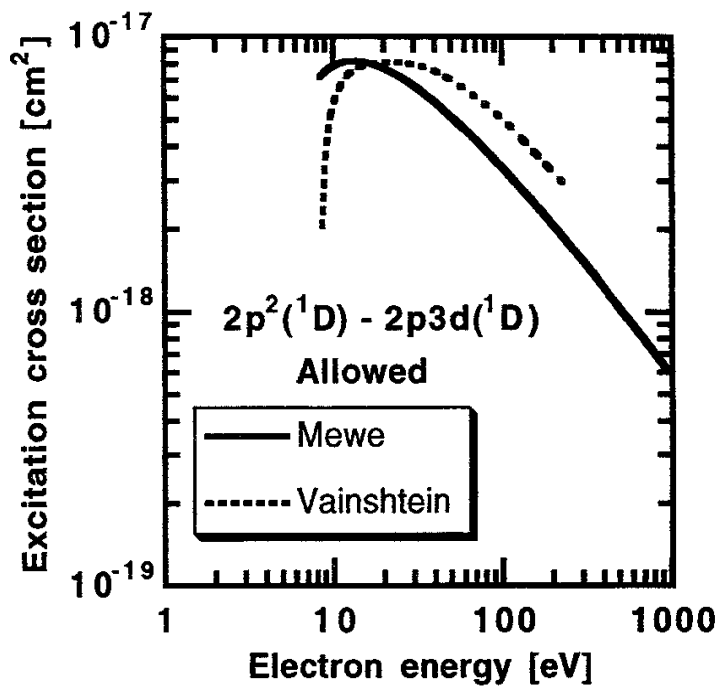


Fig. B6

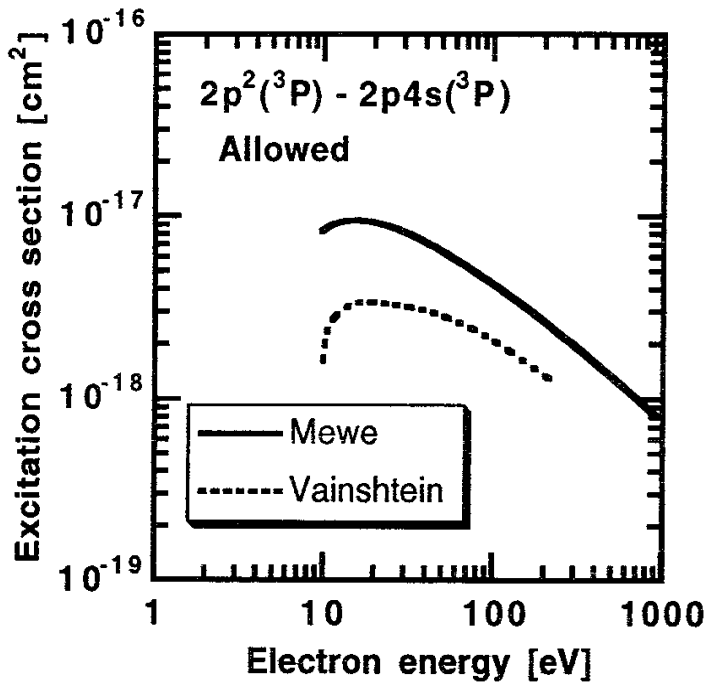


Fig. B7

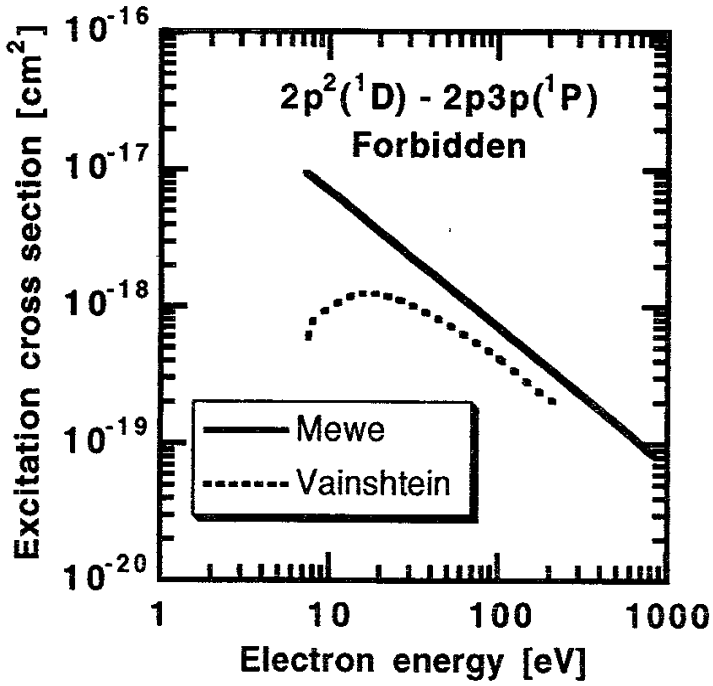


Fig. B8

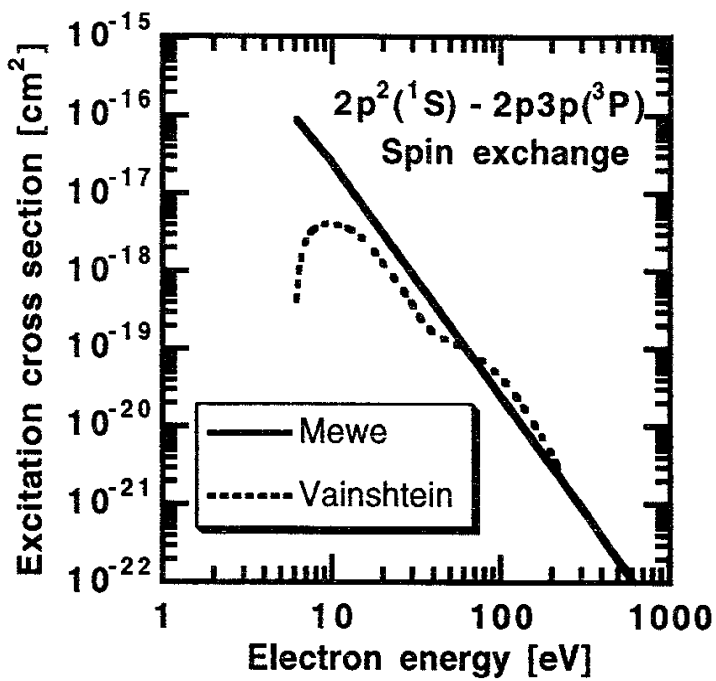


Fig. B9

Recent Issues of NIFS Series

- NIFS-182 K. Itoh, H. Sanuki and S.-I. Itoh, *Effect of Alpha Particles on Radial Electric Field Structure in Torsatron / Heliotron Reactor*; Sep. 1992
- NIFS-183 S. Morimoto, M. Sato, H. Yamada, H. Ji, S. Okamura, S. Kubo, O. Motojima, M. Murakami, T. C. Jernigan, T. S. Bigelow, A. C. England, R. S. Isler, J. F. Lyon, C. H. Ma, D. A. Rasmussen, C. R. Schaich, J. B. Wilgen and J. L. Yarber, *Long Pulse Discharges Sustained by Second Harmonic Electron Cyclotron Heating Using a 35GHz Gyrotron in the Advanced Toroidal Facility*; Sep. 1992
- NIFS-184 S. Okamura, K. Hanatani, K. Nishimura, R. Akiyama, T. Amano, H. Arimoto, M. Fujiwara, M. Hosokawa, K. Ida, H. Idei, H. Iguchi, O. Kaneko, T. Kawamoto, S. Kubo, R. Kumazawa, K. Matsuoka, S. Morita, O. Motojima, T. Mutoh, N. Nakajima, N. Noda, M. Okamoto, T. Ozaki, A. Sagara, S. Sakakibara, H. Sanuki, T. Seki, T. Shoji, F. Shimbo, C. Takahashi, Y. Takeiri, Y. Takita, K. Toi, K. Tsumori, M. Ueda, T. Watari, H. Yamada and I. Yamada, *Heating Experiments Using Neutral Beams with Variable Injection Angle and ICRF Waves in CHS* ; Sep. 1992
- NIFS-185 H. Yamada, S. Morita, K. Ida, S. Okamura, H. Iguchi, S. Sakakibara, K. Nishimura, R. Akiyama, H. Arimoto, M. Fujiwara, K. Hanatani, S. P. Hirshman, K. Ichiguchi, H. Idei, O. Kaneko, T. Kawamoto, S. Kubo, D. K. Lee, K. Matsuoka, O. Motojima, T. Ozaki, V. D. Pustovitov, A. Sagara, H. Sanuki, T. Shoji, C. Takahashi, Y. Takeiri, Y. Takita, S. Tanahashi, J. Todoroki, K. Toi, K. Tsumori, M. Ueda and I. Yamada, *MHD and Confinement Characteristics in the High- β Regime on the CHS Low-Aspect-Ratio Heliotron / Torsatron* ; Sep. 1992
- NIFS-186 S. Morita, H. Yamada, H. Iguchi, K. Adati, R. Akiyama, H. Arimoto, M. Fujiwara, Y. Hamada, K. Ida, H. Idei, O. Kaneko, K. Kawahata, T. Kawamoto, S. Kubo, R. Kumazawa, K. Matsuoka, T. Morisaki, K. Nishimura, S. Okamura, T. Ozaki, T. Seki, M. Sakurai, S. Sakakibara, A. Sagara, C. Takahashi, Y. Takeiri, H. Takenaga, Y. Takita, K. Toi, K. Tsumori, K. Uchino, M. Ueda, T. Watari, I. Yamada, *A Role of Neutral Hydrogen in CHS Plasmas with Reheat and Collapse and Comparison with JIPP T-IIU Tokamak Plasmas* ; Sep. 1992
- NIFS-187 K. Itoh, S.-I. Itoh, A. Fukuyama, M. Yagi and M. Azumi, *Model of the L-Mode Confinement in Tokamaks* ; Sep. 1992
- NIFS-188 K. Itoh, A. Fukuyama and S.-I. Itoh, *Beta-Limiting Phenomena in High-Aspect-Ratio Toroidal Helical Plasmas*; Oct. 1992

- NIFS-189 K. Itoh, S. -I. Itoh and A. Fukuyama, *Cross Field Ion Motion at Sawtooth Crash* ; Oct. 1992
- NIFS-190 N. Noda, Y. Kubota, A. Sagara, N. Ohyaibu, K. Akaishi, H. Ji, O. Motojima, M. Hashiba, I. Fujita, T. Hino, T. Yamashina, T. Matsuda, T. Sogabe, T. Matsumoto, K. Kuroda, S. Yamazaki, H. Ise, J. Adachi and T. Suzuki, *Design Study on Divertor Plates of Large Helical Device (LHD)* ; Oct. 1992
- NIFS-191 Y. Kondoh, Y. Hosaka and K. Ishii, *Kernel Optimum Nearly-Analytical Discretization (KOND) Algorithm Applied to Parabolic and Hyperbolic Equations* : Oct. 1992
- NIFS-192 K. Itoh, M. Yagi, S.-I. Itoh, A. Fukuyama and M. Azumi, *L-Mode Confinement Model Based on Transport-MHD Theory in Tokamaks* ; Oct. 1992
- NIFS-193 T. Watari, *Review of Japanese Results on Heating and Current Drive* ; Oct. 1992
- NIFS-194 Y. Kondoh, *Eigenfunction for Dissipative Dynamics Operator and Attractor of Dissipative Structure* ; Oct. 1992
- NIFS-195 T. Watanabe, H. Oya, K. Watanabe and T. Sato, *Comprehensive Simulation Study on Local and Global Development of Auroral Arcs and Field-Aligned Potentials* ; Oct. 1992
- NIFS-196 T. Mori, K. Akaishi, Y. Kubota, O. Motojima, M. Mushiaki, Y. Funato and Y. Hanaoka, *Pumping Experiment of Water on B and LaB₆ Films with Electron Beam Evaporator* ; Oct., 1992
- NIFS-197 T. Kato and K. Masai, *X-ray Spectra from Hinotori Satellite and Suprathermal Electrons* ; Oct. 1992
- NIFS-198 K. Toi, S. Okamura, H. Iguchi, H. Yamada, S. Morita, S. Sakakibara, K. Ida, K. Nishimura, K. Matsuoka, R. Akiyama, H. Arimoto, M. Fujiwara, M. Hosokawa, H. Idei, O. Kaneko, S. Kubo, A. Sagara, C. Takahashi, Y. Takeiri, Y. Takita, K. Tsumori, I. Yamada and H. Zushi, *Formation of H-mode Like Transport Barrier in the CHS Heliotron / Torsatron* ; Oct. 1992
- NIFS-199 M. Tanaka, *A Kinetic Simulation of Low-Frequency Electromagnetic Phenomena in Inhomogeneous Plasmas of Three-Dimensions* ; Nov. 1992
- NIFS-200 K. Itoh, S.-I. Itoh, H. Sanuki and A. Fukuyama, *Roles of Electric Field on Toroidal Magnetic Confinement*, Nov. 1992

- NIFS-201 G. Gnudi and T. Hatori, *Hamiltonian for the Toroidal Helical Magnetic Field Lines in the Vacuum*; Nov. 1992
- NIFS-202 K. Itoh, S.-I. Itoh and A. Fukuyama, *Physics of Transport Phenomena in Magnetic Confinement Plasmas*; Dec. 1992
- NIFS-203 Y. Hamada, Y. Kawasumi, H. Iguchi, A. Fujisawa, Y. Abe and M. Takahashi, *Mesh Effect in a Parallel Plate Analyzer*; Dec. 1992
- NIFS-204 T. Okada and H. Tazawa, *Two-Stream Instability for a Light Ion Beam-Plasma System with External Magnetic Field*; Dec. 1992
- NIFS-205 M. Osakabe, S. Itoh, Y. Gotoh, M. Sasao and J. Fujita, *A Compact Neutron Counter Telescope with Thick Radiator (Cotetra) for Fusion Experiment*; Jan. 1993
- NIFS-206 T. Yabe and F. Xiao, *Tracking Sharp Interface of Two Fluids by the CIP (Cubic-Interpolated Propagation) Scheme*, Jan. 1993
- NIFS-207 A. Kageyama, K. Watanabe and T. Sato, *Simulation Study of MHD Dynamo : Convection in a Rotating Spherical Shell*; Feb. 1993
- NIFS-208 M. Okamoto and S. Murakami, *Plasma Heating in Toroidal Systems*; Feb. 1993
- NIFS-209 K. Masai, *Density Dependence of Line Intensities and Application to Plasma Diagnostics*; Feb. 1993
- NIFS-210 K. Ohkubo, M. Hosokawa, S. Kubo, M. Sato, Y. Takita and T. Kuroda, *R&D of Transmission Lines for ECH System* ; Feb. 1993
- NIFS-211 A. A. Shishkin, K. Y. Watanabe, K. Yamazaki, O. Motojima, D. L. Grekov, M. S. Smirnova and A. V. Zolotukhin, *Some Features of Particle Orbit Behavior in LHD Configurations*; Mar. 1993
- NIFS-212 Y. Kondoh, Y. Hosaka and J.-L. Liang, *Demonstration for Novel Self-organization Theory by Three-Dimensional Magnetohydrodynamic Simulation*; Mar. 1993
- NIFS-213 K. Itoh, H. Sanuki and S.-I. Itoh, *Thermal and Electric Oscillation Driven by Orbit Loss in Helical Systems*; Mar. 1993
- NIFS-214 T. Yamagishi, *Effect of Continuous Eigenvalue Spectrum on Plasma Transport in Toroidal Systems*; Mar. 1993
- NIFS-215 K. Ida, K. Itoh, S.-I. Itoh, Y. Miura, JFT-2M Group and A. Fukuyama, *Thickness of the Layer of Strong Radial Electric Field in JFT-2M*

H-mode Plasmas; Apr. 1993

- NIFS-216 M. Yagi, K. Itoh, S.-I. Itoh, A. Fukuyama and M. Azumi, *Analysis of Current Diffusive Ballooning Mode; Apr. 1993*
- NIFS-217 J. Guasp, K. Yamazaki and O. Motojima, *Particle Orbit Analysis for LHD Helical Axis Configurations ; Apr. 1993*
- NIFS-218 T. Yabe, T. Ito and M. Okazaki, *Holography Machine HORN-I for Computer-aided Retrieve of Virtual Three-dimensional Image ; Apr. 1993*
- NIFS-219 K. Itoh, S.-I. Itoh, A. Fukuyama, M. Yagi and M. Azumi, *Self-sustained Turbulence and L-Mode Confinement in Toroidal Plasmas ; Apr. 1993*
- NIFS-220 T. Watari, R. Kumazawa, T. Mutoh, T. Seki, K. Nishimura and F. Shimpo, *Applications of Non-resonant RF Forces to Improvement of Tokamak Reactor Performances Part I: Application of Ponderomotive Force ; May 1993*
- NIFS-221 S.-I. Itoh, K. Itoh, and A. Fukuyama, *ELMy-H mode as Limit Cycle and Transient Responses of H-modes in Tokamaks ; May 1993*
- NIFS-222 H. Hojo, M. Inutake, M. Ichimura, R. Katsumata and T. Watanabe, *Interchange Stability Criteria for Anisotropic Central-Cell Plasmas in the Tandem Mirror GAMMA 10 ; May 1993*
- NIFS-223 K. Itoh, S.-I. Itoh, M. Yagi, A. Fukuyama and M. Azumi, *Theory of Pseudo-Classical Confinement and Transmutation to L-Mode; May 1993*
- NIFS-224 M. Tanaka, *HIDENEK: An Implicit Particle Simulation of Kinetic-MHD Phenomena in Three-Dimensional Plasmas; May 1993*
- NIFS-225 H. Hojo and T. Hatori, *Bounce Resonance Heating and Transport in a Magnetic Mirror; May 1993*
- NIFS-226 S.-I. Itoh, K. Itoh, A. Fukuyama, M. Yagi, *Theory of Anomalous Transport in H-Mode Plasmas; May 1993*
- NIFS-227 T. Yamagishi, *Anomalous Cross Field Flux in CHS Torsatron; May 1993*